Active Density Pattern Formation in Bacterial Binary Mixtures

Silvia Espada Burriel◉ and Remy Colin◉*

Max Planck Institute for Terrestrial Microbiology, Karl-von-Frisch-strasse 10, 35043 Marburg, Germany

Microbial communities often exhibit complex spatial structures that are important for their functioning, ecology, and evolution. While the role of biochemical interactions is extensively studied, how physical interactions contribute to structuring typically multispecies and phenotypically diverse bacterial communities is unclear. Here, we examined how motility, a major bacterial trait, affects the organization of model binary mixtures of motile and nonmotile *Escherichia coli* bacteria, revealing a novel type of active self-organization. Motile bacteria induce large-scale, fluctuating density patterns in nonmotile bacteria across a wide range of physiologically relevant cell densities. Combining experiments and quantitative modeling, we demonstrate that this pattern formation solely results from physical interactions and relies on two key ingredients: By swimming in circles at surfaces, the motile bacteria generate recirculating hydrodynamic flows that advect nonmotile cells, and the breaking of vertical symmetry by gravity permits local density accumulation. The density patterns fluctuate as the advection landscape slowly rearrange with motile cells configurations on the surfaces. This new nonequilibrium mechanism for pattern formation in bacteria belongs to a different class compared to previous models for self-organization in self-propelled systems, which rely on localized traffic jamming in two dimensions. It is instead similar to fluctuation-dominated phase ordering in active nematics. The behavior also drives the formation of large scale and highly structured aggregates of nonmotile cells that express adhesins in the mixture, and it showcases how motile species activity can shape the spatial organization of complex microbial communities.

I. INTRODUCTION

Natural microbial communities are composed of multiple phenotypically diverse species that organize in a wide variety of complex spatial structures [1–3]. This complex organization is thought to be a prominent determinant for their coexistence, ecology, and evolution [2–4]. Biochemical interactions between species are known to shape the structure of microbial communities, especially when the colony forms a sessile (nonmotile) surface attached biofilm [5–7]. While having been much less investigated, physical interactions between phenotypically different species have also been proposed to strongly affect population organization, particularly where active motility is involved.

Many bacterial species, including the model organism *Escherichia coli*, indeed swim by rotating helical flagella that propel them at speeds of ∼10–100 μm/s. At the single-cell level, the bacterium alternates seconds-long straight runs (modulo rotational Brownian motion) with short reorientations, the tumbles, to describe an exploratory random walk [8]. This motility is coupled to a sensory system, the chemotaxis

pathway, which modulates the tumbling frequency in response to physicochemical cues to navigate through the environment [9–12].

Bacterial suspensions are active fluids, which are driven out of equilibrium by swimmers constantly pouring mechanical energy into the fluid. As a result, a host of self-organization behaviors may take place from the single cell to population levels [13]. The bacteria can be thought of as force dipoles in a low Reynolds number fluid [14] which interact hydrodynamically with each other and with surfaces at long range via the fluid they displace, on top of steric interactions upon direct collisions [15]. At the single-cell level, swimming bacteria tend to accumulate near surfaces due to both types of interactions [16–20]. The proximity to the surface also alters their swimming behavior, making them swim in circular trajectories [21–23].

In homogeneous motile bacterial populations, hydrodynamic and steric interactions between the rod-shaped bacteria induce polar ordering, which explains the emergence of swirling collective motion known as bacterial turbulence at high volume fractions, $\phi > 1\%$ [24–28]. In contrast, if speed decreases when density gets high, a motility-induced phase separation (MIPS) can take place, where the active fluid phase-separates in slow dense and fast sparse regions [29–31]. In the case of active Brownian particles, MIPS can arise because of such local traffic jamming via steric interactions [30,32]. In bacteria, hydrodynamics-induced polar alignment prevents swimming speed from decreasing at high density [27], but MIPS can result from density-induced biological

---

*Corresponding author:
remy.colin@synmikro.mpi-marburg.mpg.de

downregulation of motility [33]. Chemotactic motility towards quorum-sensing chemicals released by other cells can also produce density patterns [34], ranging in bacteria from 100 μm large aggregates [35] to both static and dynamic structures on a 1–10 mm scale [36–39].

In heterogeneous mixtures of motile cells and nonmotile (passive) agents, a few nonequilibrium effects have been observed. Motile cells are known to enhance the diffusion of passive particles [40–42], notably affecting their sedimentation [43,44]. Large passive Brownian colloids may also experience effective attractive interactions when in suspension with motile cells [45–47]. Moreover, numerical simulations of mixtures of active and passive Brownian particles have shown the emergence of spatial coorganization patterns in two dimensions, both for disks [48–53] and rods [54]. The passive particles form dynamic clusters driven by the activity of the motile particles, which cosegregate, in a mechanism reminiscent of MIPS [55]. Active particles with different mobilities also seem to demix [56,57]. When passive particles are coupled to an active nematic, which commonly models dense active actin filament suspensions rather than bacteria [58], a fluctuation-dominated phase ordering (FDPO) has been observed in simulations, where density fluctuations of the passive particles emerge as they surf on the two-dimensional active nematic [59–61]. Experimentally, few studies have investigated self-organization in bacterial mixtures, although it has been observed when motility is coupled to biochemical interactions, e.g., when two strains cross-regulate each other's motility [62] or compete for resources [63], when a nonmotile strain recruits a motile one in its biofilm via chemotaxis [64], or when a nonmotile strain hitchhikes with a motile one [65]. However, it has remained unclear whether the sole physics of motility can lead to patterns in such bacterial mixtures.

Here, we investigated the physical effect of motility on the spatial organization of complex communities, using binary mixtures of bacteria, where one component is motile and the other is not, as a minimal model system. We observe that large spatial heterogeneities of the nonmotile cell density emerge under the action of the motile cells, which themselves remain homogeneous. These density patterns form on a wide range of biologically relevant densities of both phenotypes, and they induce complex large-scale aggregation structures for adhesin-expressing cells, indicating that they can affect complex natural community structures. Our experiments found that the density heterogeneities emerge because, on average, surface-localized swimmers generate three-dimensional recirculation flows that advect the nonmotile cells. The advection fluxes then combine with top-down symmetry breaking by sedimentation to allow for local cell accumulation and thus pattern formation. Our numerical simulations fully supported this new type of pattern formation mechanism in self-propelled systems.

II. EMERGENCE OF LARGE-SCALE DENSITY PATTERNS IN BACTERIAL BINARY MIXTURES

We focus on the physical effects of motility in a phenotypically diverse bacterial population. To reduce the complexity compared to natural microbial communities, we adopted a minimal model system, i.e., a binary mixture of two phenotypes: a motile and a nonmotile strain of the bacterium *E. coli*. For simplicity, the strains are nonaggregating (knockout of the adhesin Ag43) and genetically identical, except for the knockout of the flagellar filament gene *fliC* in the nonmotile one and their tagging with different fluorescent markers. Although minimalist, our system is directly biologically relevant, because many bacterial communities feature a mix of motile and nonmotile subpopulations, which can even spontaneously emerge in clonal populations of many commensal and pathogenic bacteria [12]. After separate growth, we mix the strains in various proportions in a no-growth medium, and we observe them under the microscope in a microfabricated chamber [Fig. 1(a)].

In a wide range of densities of both components of the binary mixture, we observed large spatial fluctuations of the density of the nonmotile cells in the presence of motile cells [Fig. 1(b)]. After a freshly stirred mixture is loaded into the chamber, it takes 15–30 min for the patterns to fully develop; see Supplemental Movie 1 [66]. In the resulting steady state, the density patterns are dynamic, showing patches of abnormally high and low densities of nonmotile cells that reorganize in a matter of minutes; see Supplemental Movies 2 and 3 [66]. Interestingly, the spatial distribution of the motile cells always remains homogeneous [Fig. 1(c)], and their swimming speed remains unchanged. The swimming activity is, however, necessary for the nonmotile density patterns to form, since the passive control system, where two differentially tagged nonmotile strains are mixed in the same proportions, is homogeneous [Fig. 1(d)]. The motile cells thus drive, by their swimming, the emergence of out-of-equilibrium density patterns for the nonmotile cells, without being themselves affected in any obvious way. This is in strong contrast to the behavior in simulated MIPS-like phase separation of passive-active mixtures [29,30,50–55], suggesting that a different pattern formation mechanism is at play.

We quantified the patterns using fluorescence intensity as a proxy for cell density; see the Methods section. The nonmotile cell density shows nonexponentially decaying spatial correlations over typical sizes of 10–50 μm, much larger than the ∼2 μm cell length, and other characteristics of giant number fluctuations [see the Supplemental Material (SM) [66], Fig. S1]. The typical pattern size was fairly constant across experimental conditions [see the SM [66], Figs. S1(d) and S1(e)]. We thus characterized the magnitude of the phenomenon through the heterogeneity level, i.e., the amplitude of the density fluctuations. It was quantified via the spatial variance of the cell density, coarse-grained on the typical pattern size; see the Methods section. After sample loading, the heterogeneity level increases slightly faster at higher motile cell density, but always reaches steady state within $t \sim 30$ min (SM [66], Fig. S2). We constructed the full phase diagram of the heterogeneity level at steady state (i.e., $t \simeq 1$ h) as a function of the volume fractions of motile (ϕ_M) and nonmotile (ϕ_{NM}) cells [Fig. 1(e)]; see also the SM [66], Fig. S3. A heterogeneity level above the passive control value is observed only for nonmotile cells, when they are in a majority ($\phi_{NM} > \phi_M$). It reaches a maximum for $\phi_{NM} \simeq 5\%$ and $\phi_M \simeq 0.2\%$. This is far below the onset of swirling collective motion for $\phi_M \gtrsim 1\%$ [24,27,28], where the heterogeneity level of the nonmotile
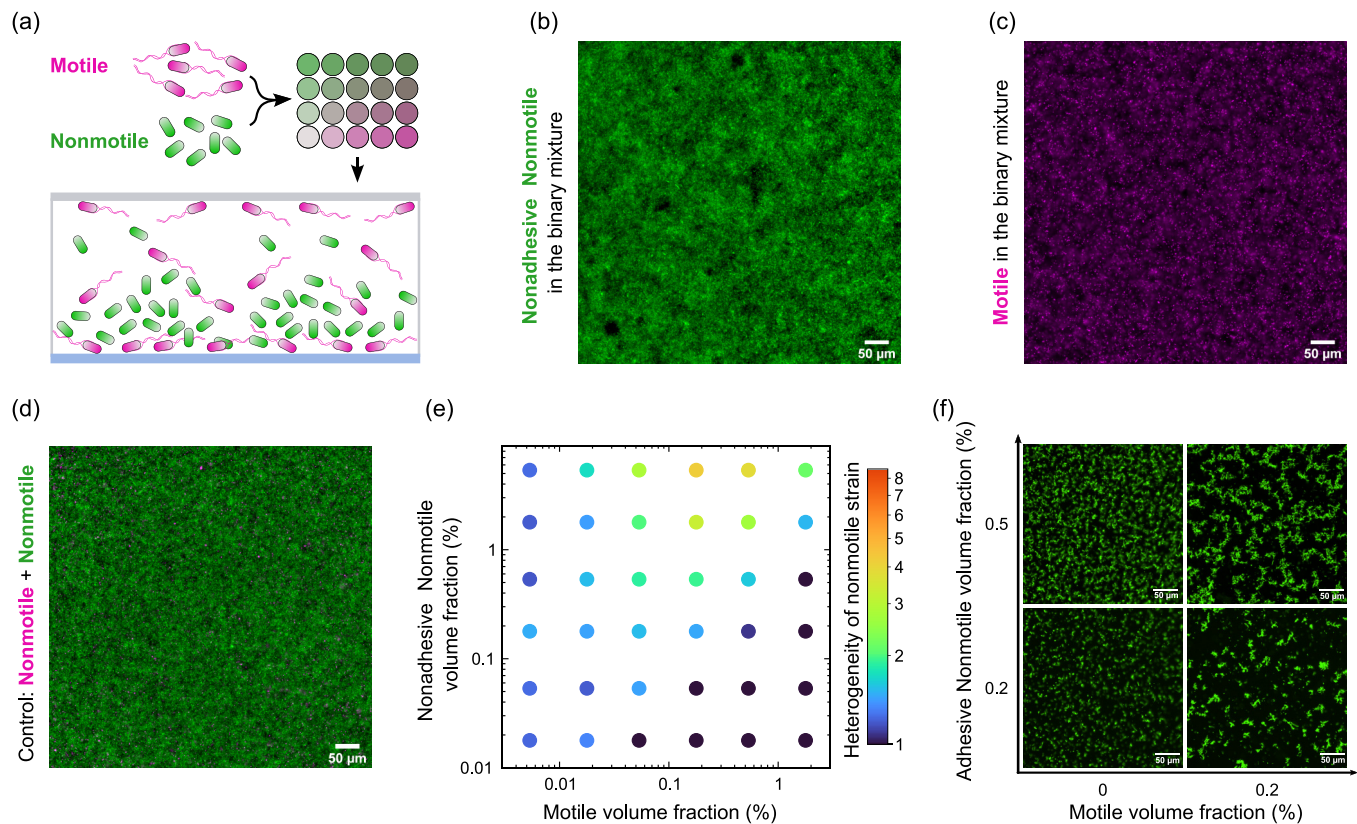
FIG. 1. Nonequilibrium density patterns in bacterial binary mixtures. (a) Scheme of the binary mixture experiment, featuring differently tagged motile and nonmotile *E. coli* strains mixed in various proportions after separate growth. (b) Microscopy images of mNeonGreen-tagged nonmotile *E. coli* strain in a bacterial mixtures with a motile *E. coli* strain (motile cells volume fraction $\phi_M = 0.18\%$, nonmotile $\phi_{NM} = 5.3\%$), measured 8 μm above the bottom of the 50 μm high experimental chamber. (c) Microscopy images of the mCherry-tagged motile *E. coli* strain in the same conditions as (b). (d) Microscopy images of the control where two differently tagged nonmotile strains of *E. coli* were mixed at the same volume fractions in the same conditions. (e) Phase diagram of the density heterogeneities of the nonmotile strain in binary mixtures with a motile one as a function of the volume fraction of both strains. The color scale represents the heterogeneity level. Each point represents the geometric mean of at least three biological replicates. (f) Aggregation of adhesive nonmotile cells alone ($\phi_M = 0\%$) or in mixture with $\phi_M = 0.2\%$ motile cells. Images are taken 80 min after sample preparation.

strain actually starts decreasing. The patterns are observed over a range of densities that are typical of planktonic cultures for the motile cells ($0.01 < \phi_M < 1\%$) and of biofilms for the nonmotile ones ($0.1 < \phi_{NM} < 10\%$), indicating that this phenomenon can be highly relevant to natural bacterial communities.

Consequently, we investigated whether motile cells also affect the aggregation of adhesive nonmotile cells, a first step for biofilm formation and community establishment. We substituted the nonmotile strain that we had engineered not to aggregate with one that does express the adhesin Ag43. When mixed with (nonadhesive) motile cells, these adhesive nonmotile cells rapidly form much larger and more structured aggregates than when they are alone and just subject to thermal motion [Fig. 1(f)]. This enhanced aggregation happens in the same range of motile cell density as the density patterns in the absence of aggregation [Fig. 1(e)]. These results show that the motility-induced patterns are important for the structure of microbial communities. We thus investigated the pattern formation mechanism, only using nonaggregating nonmotile cells from now on for simplicity.

III. PERSISTENCE OF CIRCULAR SWIMMING AT SURFACES CONTROLS THE LEVEL OF DENSITY HETEROGENEITIES

Motivated by chemotaxis being known to drive the formation of some bacterial density patterns [35–39,64,65], we disabled this function in the motile strain. To this end, we knocked out the gene *cheY*, which encodes the protein that carries chemosensory signals through the cell and modulates tumbling rate. To our surprise, when mixed with this nontumbling and nonchemotactic $\Delta cheY$ motile strain, the density heterogeneities of the nonmotile strain were found to be stronger and to appear on a wider range of cell densities [Figs. 2(a)–2(c)] than when the motile strain is wild-type (WT) for chemotaxis [Fig. 1(e)]. Although the typical size of the density patterns is largely unaffected [SM [66], Figs. S1(d) and S1(e)], the local extrema of density are much more accentuated, with numerous depletion zones forming next to very dense patches and spanning the whole height of the channel [Fig. 2(a); SM [66], Figs. S4(a) and S4(b)]; see Supplemental Movies 4 and 5. However, a heterogeneity level similar to the
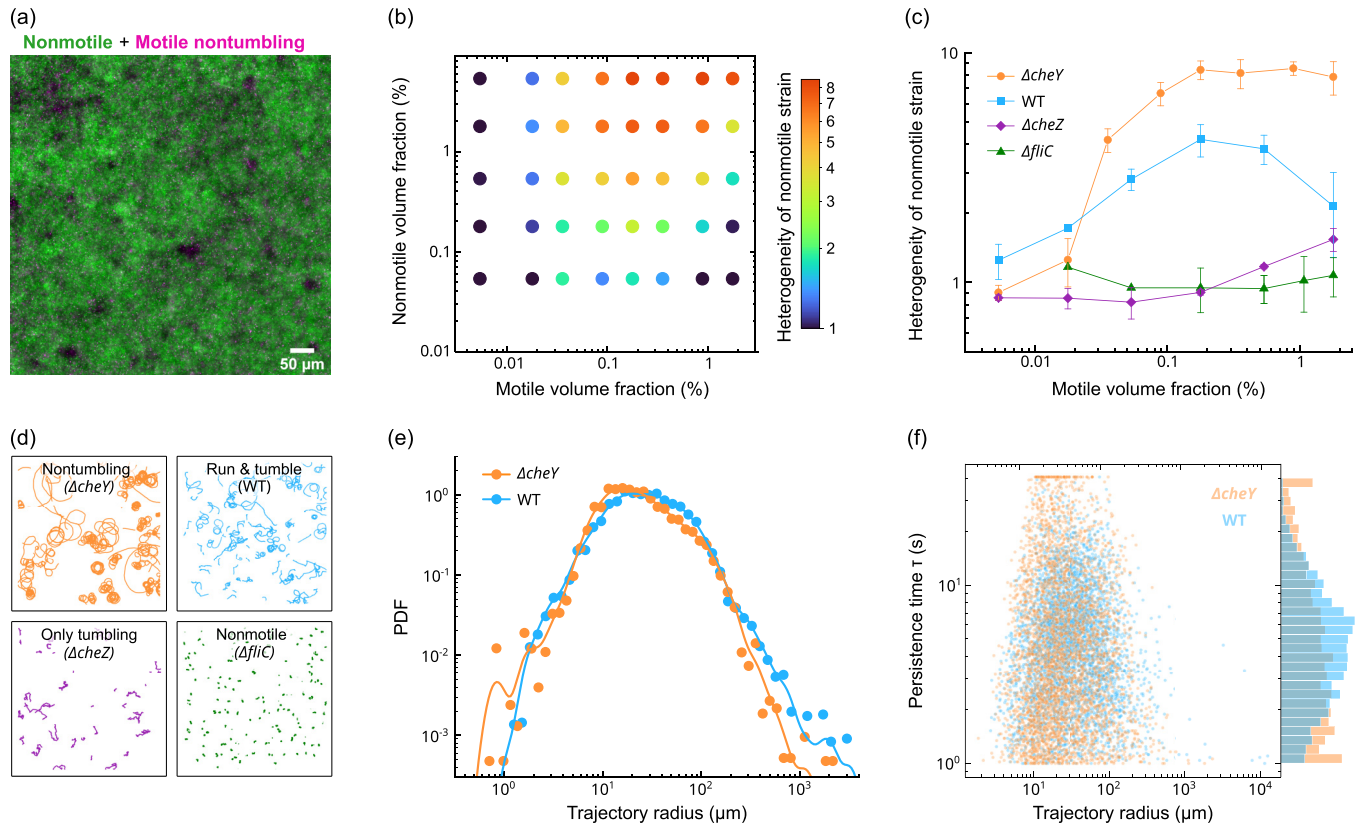
FIG. 2. Tumbling affects the density heterogeneities through the persistence of surface swimming. (a) Microscopy image of *E. coli* mixtures of a motile nontumbling strain ($\Delta cheY$ mCherry, $\phi_M = 0.18\%$) and a nonmotile strain (mNeonGreen, $\phi_{NM} = 5.3\%$), at 8 μm above the bottom of the chamber, featuring heterogeneous patterns of nonmotile cell density. (b) Phase diagram of the density fluctuations in mixtures of a nontumbling motile strain ($\Delta cheY$) (volume fraction in abscissa) with a nonmotile strain (volume fraction in ordinate). The color scale representing the heterogeneity level is the same as that in Fig. 1(e). (c) Heterogeneity levels of the nonmotile cells in a binary mixture with indicated motile strains, as a function of their volume fraction. The volume fraction of the nonmotile strain is kept constant ($\phi_{NM} = 5.3\%$). (b),(c) Each point represents the geometric mean of three replicates. (c) Error bars indicate the standard deviation. (d) Trajectories of the different strains used as the motile strain in the binary mixtures, which were tracked at the bottom of the experimental chamber. (e) Probability density distribution of the radii of curvature of individual circular swimming trajectories of WT and $\Delta cheY$ motile cells. Lines represent kernel density estimates. (f) Scatter plot of the persistence time τ of the same trajectories as (e), as a function of the radius of curvature of the trajectory, and probability density distribution of τ (right side). (e),(f) The data set comprises 4137 ($\Delta cheY$) and 4475 (WT) individual swimming trajectories in eight biological replicates.

WT strain case was found across the whole phase diagram for the motile *cheY*** mutant [SM [66], Fig. S4(c)], which has a WT level of tumbling but no chemotactic response [67]. It is therefore not chemotaxis *per se*, but rather the ability to tumble that controls the heterogeneity level. Moreover, almost identical density patterns were observed when substituting the nonmotile strain with fluorescently labeled passive colloids of similar size [SM [66], Figs. S4(f) and S4(g)]. These results strongly indicate that pattern formation results from purely physical interactions, which are modulated by tumbling.

The latter is known to strongly affect swimming behavior close to surfaces. It not only helps escaping entrapment at surfaces [17,18,20], but it also perturbs the patterns of swimming in circles at the surface [21,23]. In our system, both WT and $\Delta cheY$ motile cells primarily localize close to the top and bottom surfaces, this localization being only moderately enhanced in the $\Delta cheY$ case [SM [66], Fig. S4(d)]. The circular swimming patterns at the surface are more strongly

affected [Fig. 2(d)]. As quantified by cell tracking, the WT and nontumbling strains showed almost identical, very broad distributions of radii of curvature R of their circular trajectories [Fig. 2(e)]. This broadness is not unexpected since R depends strongly on the variable distance between the cell and the surface [21,22]. However, the circles persist in place much longer in the $\Delta cheY$ strain, where only diffusion perturbs them, than in the WT strain, because of reorientations via tumbles [Fig. 2(d)]. The distribution of circle persistence times—the time τ needed for a cell to "break the circle," i.e., to translate by $\delta r(\tau) \geqslant 3R$—is indeed strongly upshifted for the $\Delta cheY$ strain, where a large fraction of cells stay in the $3R$ vicinity for the whole duration (40 s) of the cell tracking movie [Fig. 2(f)]. Conversely, we then drastically reduced the persistence of swimming by considering a tumbling-only motile strain, $\Delta cheZ$, for which flagella rotate only clockwise, causing constant tumbling and almost Brownian-like motion [Fig. 2(d)], while still pouring energy into the fluid. The

heterogeneity level of the nonmotile strain of the mixture drops to almost control levels for all tumbling-only volume fractions [Fig. 2(c)]. These results indicate that persistent swimming in circles at the surface of the motile cells is a first key driver of the emergence of the nonmotile cell density patterns.

We also perturbed the circular swimming patterns by elongating both motile strains with the antibiotic cephalexin [27]. The radii of curvature of elongated cell trajectories increase on average, as expected from theory [21], but their distribution remains broad, likely due to the varying distances to the surface [SM [66], Figs. S5(a)–S5(c)]. The typical circle persistence time was mostly unchanged ($\Delta cheY$) or increased slightly (WT), as did the heterogeneity level of the nonmotile cells, compared to the mixtures with normal-sized swimmers at equal volume fractions [SM [66], Figs. S5(d)–S5(f)]. This result is somewhat unexpected because the number density of elongated motile cells is then twice as small, but it likely stems from elongated cells having a larger hydrodynamic dipole strength, among other factors we will discuss further on.

IV. SPATIOTEMPORALLY STRUCTURED FLUID FLOWS GENERATED BY THE MOTILE CELLS ADVECT THE NONMOTILE ONES

We hypothesized that the motile cells swimming in a circle at the surface reorganize the nonmotile cells into heterogeneous patterns. We thus studied nonmotile cell dynamics in the mixtures at steady state; see Supplemental Movies 2–5 [66]. The nonmotile cells show collective movements with many converging and diverging convective flows. The movements are more pronounced when motile cells do not tumble, with cell depletion zones ("holes") intermittently opening and closing on a minutes timescale. We quantified the horizontal nonmotile cell motion by particle image velocimetry (PIV), measuring their velocities over a 2 s timescale [Figs. 3(a) and 3(b)]. Even at volume fractions of motile cells far below the emergence of bacterial turbulence, the velocity fields revealed large spatial correlations in the motion of nonmotile cells [Fig. 3(a)]. We quantified them via the normalized spatial power spectral density of the velocity field, $E(q) = q|\tilde{v}(q)|^2/\langle v^2 \rangle$, which depends on the spatial wave number q and represents the fraction of the kinetic energy ($\langle v^2 \rangle$) in flow structures of typical size π/q [26,27]. In the presence of motile cells, $E(q)$ shows a pronounced peak, the hallmark of spatial correlation, at a wavelength $\pi/q = 50\,\mu m$, corresponding to the height of the channel [Fig. 3(b)]. This value indicates that hydrodynamic interactions drive these collective nonmotile cell movements, similarly to previous results for bacterial turbulence of swimmer-only systems [27]. Motile cells thus generate intermittently structured flow fields that are able to stir the nonmotile ones.

The strength of the collective flows, measured by the peak of $E(q)$ and the instantaneous kinetic energy $\langle v^2 \rangle$, however, does not predict well the heterogeneity level, as evidenced by their different dependences in the WT and $\Delta cheY$ case [SM [66], Figs. S6(a) and S6(b)]. In contrast, the temporal correlations of the velocity field decayed fairly rapidly in the tumbling motile case (WT), whereas long-term (5–40 s) correlations are clearly visible in the nontumbling $\Delta cheY$ one

[Fig. 3(c)], coherently with the longer persistence of circular swimming in the latter case [Fig. 2(f)], and correspondingly to a higher level of heterogeneity. The persistence of the motile swimming patterns and hence of the flows they induce thus clearly controls the level of heterogeneity of the density patterns.

We next considered the three-dimensional structure of the nonmotile cell advection. We tracked the three-dimensional motion of a few marked nonmotile tracers with confocal microscopy in mixtures with unmarked nonmotile and nontumbling motile cells. We focused on areas where a cell depletion zone ("hole") is visible with transmitted light [Fig. 3(d)], and we quantified the velocity of the tracers as a function of the distance to the center of the hole (r) [Figs. 3(e) and 3(f)]; see also SM [66], Figs. S6(c) and S6(d). Although each individual tracer cell appears to move quite randomly due to Brownian diffusion [Figs. 3(d) and 3(f), inset], which is further enhanced by motile cell activity [SM [66], Figs. S7(a) and S7(b)], population averages reveal an underlying flow structure [Figs. 3(e) and 3(f)]. Close to the hole center ($r < 10\,\mu m$), the mean vertical velocity of the tracers is strongly negative ($\langle V_z \rangle \simeq -0.3\,\mu m/s$), indicating strong downward suction. It then increases and reaches a maximum further away from the hole ($r \sim 20\,\mu m$). The nonmotile cells also move faster than the expected diffusion flux away from the hole center in the horizontal direction ($\langle V_r \rangle > 0$). Far from the hole ($r > 30\,\mu m$), the radial velocity relative to the hole ($\langle V_r \rangle$) is zero on average, while the mean vertical velocity is consistent with the sedimentation speed of the nonmotile cells in the suspending medium ($\simeq 0.05\,\mu m/s$). These findings indicate that the nonmotile cells are exposed to a recirculatory flow generated by the circular surface swimmers, which drag them down and expel them away in the vicinity of the hole.

V. VERTICAL SYMMETRY BREAKING BY NONMOTILE CELLS SEDIMENTATION IS ESSENTIAL FOR PATTERN FORMATION

Nonmotile cells cannot become heterogeneously distributed simply by following the streamlines in an incompressible fluid. Searching for a mechanism that overcomes this effect, we noted that the nonmotile cells sediment, their volumetric mass density ($\rho_C = 1.1\,g\,cm^{-3}$) being higher than that of the aqueous medium ($\rho_W = 1.0\,g\,cm^{-3}$). Their vertical distribution, which is identical whether they are mixed with WT or $\Delta cheY$ motile cells, is a bottom-heavy Boltzmann distribution that balances sedimentation and diffusion [SM [66], Fig. S4(e)]. The latter is enhanced as the volume fraction of motile cells increases [SM [66], Figs. S7(a) and S7(b)], as previously observed [40,41,43], and the vertical distribution of nonmotile cells therefore homogenizes in the presence of an increasing density of motile cells [SM [66], Figs. S7(c) and S7(d)], which corresponds to a reduced heterogeneity [Fig. 1(e)].

We thus investigated how sedimentation affects the density fluctuations in our system, also inspired by previous works on sedimentation of high-density colloidal suspensions [68,69]. We matched the volumetric mass density of the suspending medium (ρ_M) to that of the bacteria by adding the innocuous density-matching agent iodixanol. We define the normalized
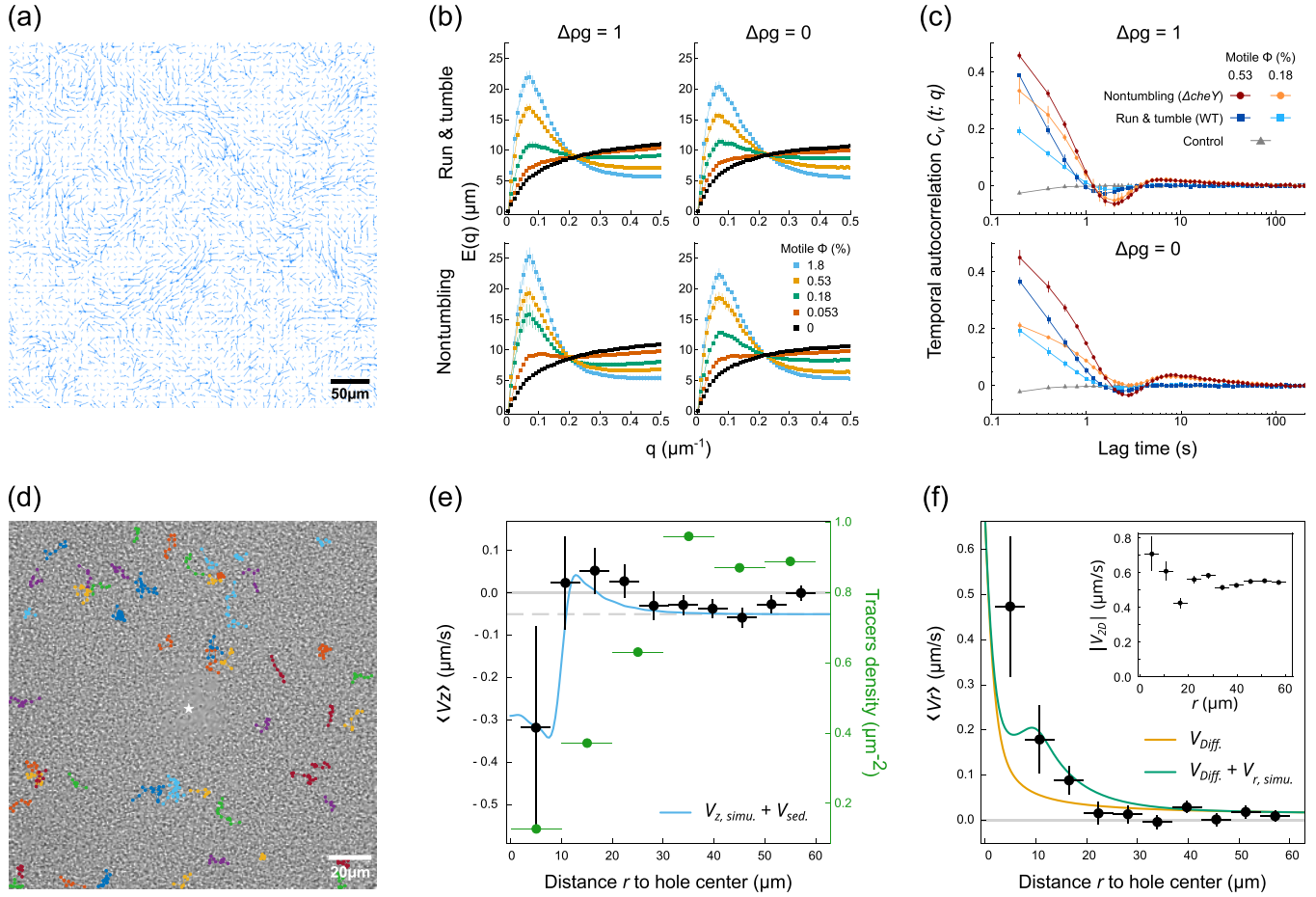
FIG. 3. Dynamics of the nonmotile cells within the density patterns. (a) Instantaneous velocity field of the nonmotile strain at $\phi_{NM} = 5.3\%$ in a mixture with the motile strain $\Delta cheY$ at $\phi_M = 0.53\%$, in the motility buffer (buoyancy $\Delta\rho g = 1$). (b) Flow structure factor $E(q)$ of the flow field of the nonmotile strain mixed with the indicated motile strains at indicated cell densities and buoyancies. (c) Temporal autocorrelation of the nonmotile cell velocity $C_v(t; q)$ as a function of the lag time t for the Fourier component of the velocity $v(q, t)$ that corresponds to the peak of $E(q)$, $q = 0.06 \, \mu m^{-1}$, in the indicated conditions. The velocity is measured on a shorter (0.2 s) time window than (a),(b) (2 s) to increase temporal resolution. (b),(c) The nonmotile cell density is $\phi_{NM} = 5.3\%$. Points indicate the mean, and error bars indicate the standard error of the mean on two biological replicates. (d) Example of the three-dimensional tracking of nonmotile cells close to a hole, performed in the mixture $\phi_{NM} = 5.3\%$, $\Delta cheY$ $\phi_M = 0.53\%$ in the motility buffer (buoyancy $\Delta\rho g = 1$). The white star represents the mean position of the hole center over the whole recording time, and the colored points represent the XY projection of the 3D trajectories of the tracers (tagged nonmotile cells). (e) Average vertical velocity of the tracers $\langle V_z \rangle$ (black circles) and their density (green circles) as a function of their distance r to a hole. (f) Average radial velocity of the tracers $\langle V_r \rangle$ (black circles) and horizontal speed $|V_{2D}| = \langle \sqrt{V_x^2 + V_y^2} \rangle$ (inset) as a function of the distance r to a hole. (e),(f) The velocities were quantified from 639 individual 3D trajectories situated less than $60 \, \mu m$ away from a hole center. Each data point represents the binned mean, and the vertical error bars represent the standard error of the mean. The continuous lines are simulated flows generated by circular swimmers ($R = 10 \, \mu m$, $a^S v_0 = 70 \, \mu m^2/s$). The blue line (d) sums the vertical flow speed from the circular trajectories ($V_{Z,simu}$) and the sedimentation speed ($V_{sed} = 0.05 \, \mu m/s$). The yellow line (e) is the radial diffusive speed (V_{Diff}), while the green line (e) sums V_{Diff} and the radial flow speed from the circular trajectories ($V_{r,simu}$).

buoyancy in the media relative to that in water as

$$\Delta\rho g = (\rho_C - \rho_M)/(\rho_C - \rho_W). \tag{1}$$

In the neutrally buoyant medium ($\Delta\rho g = 0$), the speed of motile cells, the nonmotile diffusion, and the vertical distribution of motile cells are unchanged [SM [66], Figs. S8(a)–S8(c)], but the vertical distribution of nonmotile cells becomes homogeneous, completely annihilating the heterogeneities of nonmotile cell density. They fall to a nonmotile-only control level, whether the motile strain in the mixture is tumbling or not, and no matter how high the

nonmotile cell density is [Figs. 4(a) and 4(b)]; see also SM [66], Figs. S8(d)–S8(f).

Focusing on one of the most heterogeneous mixtures in the negatively buoyant fluid ($\Delta\rho g = 1$, motile $\Delta cheY$ with $\phi_M \simeq 0.2\%$ and $\phi_{NM} \simeq 5\%$), we investigated the effect of varying the difference of volumetric mass density between the cells and the medium, i.e., the sedimentation speed, and therefore the slope of the vertical cell density profile [Fig. 4(c)]. The density heterogeneity increased as a function of this density mismatch, showing that vertical asymmetry controls the heterogeneities [Fig. 4(d)]. Matching the channel height with the scale of the vertical gradient of nonmotile cell density by
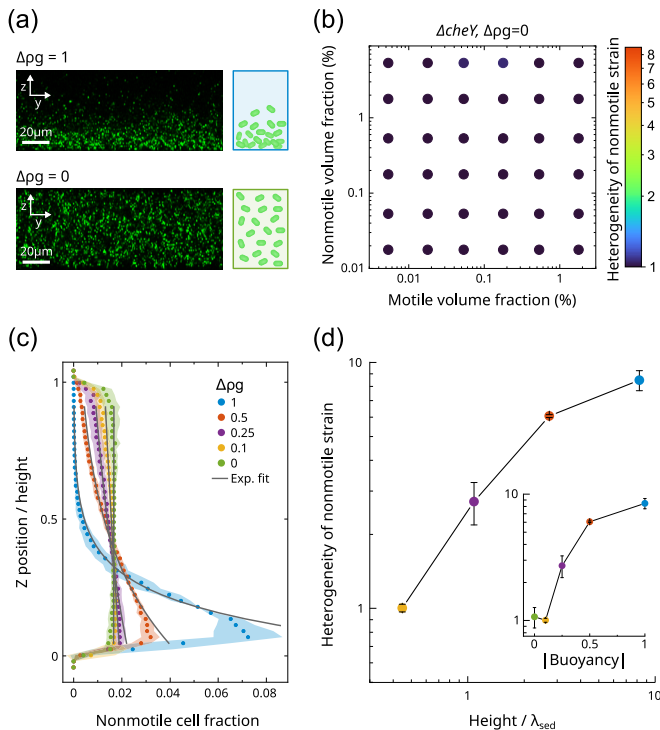
FIG. 4. Sedimentation controls the density heterogeneities. (a) Confocal images of the vertical distribution of nonmotile cells at the two extreme buoyancies $\Delta\rho g = 1$ (motility buffer) and $\Delta\rho g = 0$ (density-matched medium). (b) Phase diagram of the density fluctuations in a mixture of $\Delta cheY$ motile strain (volume fraction in abscissa) with a nonmotile strain (volume fraction in ordinate) in density-matched suspending media ($\Delta\rho g = 0$). The color scale representing the heterogeneity level is the same as that in Fig. 1(e). (c),(d) Dose-dependence effect of buoyancy on the sedimentation (c) and the density fluctuations (d) of the most heterogeneous binary mixture ($\phi_M = 0.18\%$, $\phi_{NM} = 5.3\%$, motile strain $\Delta cheY$). (c) Nonmotile cell fraction (abscissa), measured by cell counting in confocal microscopy, as a function of the vertical position (z) in a channel of 50 μm height (ordinate), for suspensions at different buoyancies, normalized to motility buffer ($\Delta\rho g$). The gray lines are exponential fits of the cell fraction as a function of z. (d) Density fluctuations of the nonmotile strain as a function (main figure) of the inverse of the exponential decay length λ_{sed} of the sedimentation profile and (inset) of the normalized buoyancy $\Delta\rho g$. (a)–(d) Each point represents the geometric mean of three replicates. Error areas (c) and bars (d) indicate the standard deviation.

confining the $\Delta\rho g = 1$ mixtures in a 20-μm-high channel also leads to a loss of heterogeneities (SM [66], Fig. S9). These results demonstrate that the vertical gradient of cell density resulting from sedimentation is a control parameter of the system.

In the density-matched medium $\Delta\rho g = 0$, the motion of the nonmotile cells showed the same spatial flow structures, with the same length scale and barely lower amplitude, as measured by the peak of $E(q)$, as those of the $\Delta\rho g = 1$ case [Fig. 3(b)]. The total amount of kinetic energy ($\langle v^2 \rangle$) is, however, somewhat lower for $\Delta\rho g = 0$ [SM [66], Fig. S6(b)]. Sedimentation, therefore, does not drive the emergence of the collective flows, although it might reinforce them. Our

experiments thus indicate that motile cells that swim persistently in a circle near surfaces always generate flows that advect the nonmotile cells vertically. Only for $\Delta\rho g \neq 0$, when sedimentation breaks vertical symmetry, do local accumulation and depletion of nonmotile cells (depending on flow direction) produce the density patterns. They then fluctuate over time as the circular swimmers slowly rearrange their positions.

VI. SIMULATIONS REVEAL THE RECIRCULATION FLOWS PRODUCED BY CIRCULAR SWIMMERS AND REPRODUCE PATTERN FORMATION

We next turned to modeling to obtain a clear picture of the average flows induced by bacteria swimming in circles at surfaces, which had not been studied so far, and to understand how they allow for density patterns emergence. We computed the fluid flow generated in three dimensions by swimmers modeled as force dipoles, using a fast algorithm [70,71] for solving Stokes flow between two no-slip walls; see the Methods section and Supplemental Notes in SM [66]. We first considered a single dipole (hydrodynamic radius a^S and swimming speed v_0) describing a perfectly circular trajectory at the bottom surface. Averaged over one revolution, the flow field it induces, $v_{1r}(r, z)/a^S v_0$, is axisymmetric around the center of the circle and features a vertical recirculation, where the fluid is sucked down in the middle of the circle to be expelled out and up on its outside [Fig. 5(a)]; see also SM [66], Figs. S10(a)–S10(f). This recirculation is powered by the net outward flux that the dipole generates perpendicular to its curved trajectory [Fig. 5(b), inset]. Hence, the recirculation flux [Eq. (A13)] is proportional to $1/R$ [Fig. 5(b)], with R being the recirculation radius [see the Methods section and SM [66], Figs. S10(g)–S10(i)], while the mean and maximum fluid speeds, respectively, scale as $1/R^3$ and $1/R^2$ [Fig. 5(c)]. The curvature of the dipole trajectory, therefore, sets the strength of the recirculation flow.

The simulated flow curves fitted well our experimental measurements close to depletion zones for a simulated circle of radius $R = 10$ μm that matches the typical apparent hole size, when accounting for sedimentation, diffusion away from the hole center, and the 3D distribution of nonmotile tracers [Figs. 3(e) and 3(f)]; see also SM [66], Figs. S10(b), S10(d), and S10(f). The only fit parameter, the reduced dipole force $f_0/6\pi\eta = a^S v_0 = 70$ μm²/s, is five times larger than expected for a single cell ($a^S = 0.7$ μm and $v_0 = 20$ μm/s for our motile cells). This discrepancy might be explained by variations of the radius R, on which v_{1r} depends strongly, and/or by several circular swimmers contributing to various degrees to the formation of the hole.

The flow fields of thousands of interlaced circular swimmers might, however, average out, leading to no net drive for heterogeneities to emerge. Nonetheless, when we account for the broad experimental distribution of circle radii [SM [66], Fig. S11(a) and the Methods section], the total average flow field $v_{tot}/(a^S v_0)$ generated by even a large population of noncorrelated swimmers does show prominent recirculation patterns [Fig. 5(d)]. Indeed, since the typical contribution of a circle of radius R_i is of order $v_{i,1r}/(a^S v_0) \propto 1/R_i^3$, even for very large numbers of swimmers, the relatively few
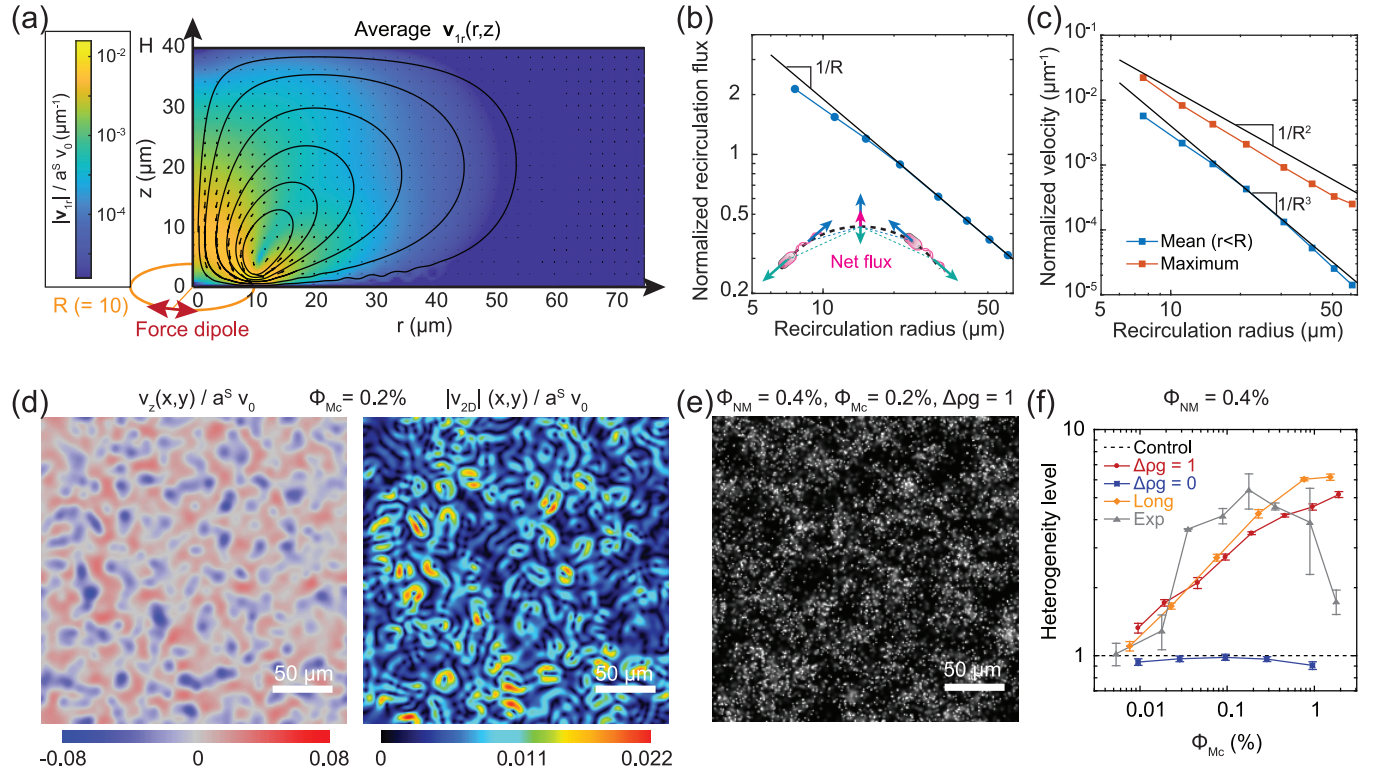
FIG. 5. Recirculation flows lead to heterogeneities of nonmotile cells in simulations of circular swimmers at surfaces. (a) Map of the axisymmetric mean flow field generated by a circularly swimming force dipole. The flow field is computed between two no-slip walls spaced by $H = 40\,\mu$m, and the dipole circulates $z_M = 0.7\,\mu$m (about one cell body) above the bottom wall. Shown are the flow speed normalized to dipole force $a^S v_0$ (color), the velocity vectors (arrows), and streamlines in the (r, z) plane (solid lines), featuring a recirculation around a fixed point close to the circle radius. (b) Normalized recirculation flux, $\max_{\{r\}} \Phi(r)/a^S v_0$ [Eq. (A13), in μm] as a function of the recirculation radius. The solid line indicates $1/R$ dependence. Inset: Scheme of the flow field generation. (c) Mean and maximum of the flow speed inside the circle as a function of the position of the fixed point (recirculation radius). Solid lines indicate power-law dependences. (d) Example of mean flow field generated by a population of circular surface swimming dipoles (density $\phi_{Mc} = 0.2\%$, $n_{Mc} = 5 \times 10^3$ circles, for which experimental heterogeneity is maximal) for the distribution of circle radii of Fig. 2(f). Trajectory centers are evenly distributed at both surfaces and independent from each other. The vertical (v_z) and horizontal ($|v_{2D}| = \sqrt{v_x^2 + v_y^2}$) components are shown in the (x, y) plane, $z = 8\,\mu$m above the bottom wall. Color scales indicate $v/a^S v_0$ in μm^{-1}. (e) Reconstructed microscopy image of negatively buoyant diffusive tracers ($v_{sed} = 0.05\,\mu$m/s, $D = 0.3\,\mu$m^2/s) that followed the mean circular swimmers flow field for 100 s, for the same conditions as (d). (f) Heterogeneity level of the nonmotile tracers, computed in simulations as a function of the volume fraction of motile circular swimmers ϕ_{Mc} for nonmotile cells (NM) with volume fraction $\phi_{NM} = 0.4\%$, for a persistence time $\tau = 60$ s. Control: homogeneous distribution; $\Delta\rho g = 1$: sedimenting NM; $\Delta\rho g = 0$: nonsedimenting NM; Long: elongated motile cells; Exp: experimental data for nontumbling motile cells, $\Delta\rho g = 1$ and $\phi_{NM} = 0.53\%$. Error bars for simulated data indicate standard error of the mean over six repeats. Experimental data encompass three biological replicates, and the error bar is standard deviation.

smaller circles in the distribution contribute massively to the total mean flow field and make it spatially heterogeneous [Fig. 5(c)]; see also SM [66], Fig. S11(b). The flow speed, using $a^S v_0 = 14\,\mu$m^2/s, is of order $v_z \sim 0.5$–$1\,\mu$m/s in the fast areas. It is now compatible with experiments [Figs. 3(e) and 3(f)] and shows that heterogeneities can arise from the flow field generated by a population of surface swimmers.

We thus computed the trajectories of passive tracers in the mean flow field generated by fixed configurations of circular swimmers with $a^S v_0 = 14\,\mu$m^2/s. The tracers experienced Brownian motion ($D = 0.3\,\mu$m^2/s) and gravity ($v_{sed} = 0.05\,\mu$m/s) at the level of nonmotile cells for $\Delta\rho g = 1$. Density patterns that are similar to the experimental ones on reconstructed images of nonmotile cells form in the same ranges of motile and nonmotile density [Fig. 5(e)]; see also SM [66], Fig. S11(c). The heterogeneity level, which is

defined comparably to experiments (see the Methods section), increases as a function of the time τ during which the tracers are exposed to a fixed circles configuration, corresponding in experiments to the circle persistence time [SM [66], Fig. S11(d)]. For τ values that are consistent with nontumbling swimmers experiments [Figs. 2(f) and 3(c)], the dependence of the simulated heterogeneity level on circular swimmer density agrees quantitatively well with experiments [Fig. 5(f)]; see also SM [66], Fig. S11(f). The simulations reproduce the complete loss of heterogeneities under neutral buoyancy, because the initial distribution of nonmotile cells is homogeneous in this case and the fluid is incompressible [Fig. 5(f)]. Normal and elongated circular swimmers also elicit equal levels of nonmotile heterogeneities [Fig. 5(f)] as in experiments with the nontumbling motile strain (SM [66], Fig. S5). Our simulations, therefore, recapitulate our

experimental results and provide a mechanism for the emergence of the density patterns in binary mixtures: Circular swimming trajectories close to surfaces generate a vertical recirculation that disturbs the asymmetric distribution of sedimenting nonmotile cells.

VII. DISCUSSION

Here, we report a new type of active collective structuring for bacteria. Fluctuating density patterns emerge in binary mixtures of motile and nonmotile bacteria, over a broad range of volume fractions of both species. We identified the purely physical mechanism of emergence, based on the combination of heterogeneous active flow fields with a symmetry breaking by gravity. Our experiments and modeling indeed demonstrate that persistent circular swimming of the motile cells at the surfaces of the sample creates, on average, recirculation fluid flows, which advect the nonmotile species in three dimensions. At population level, the flows remain heterogeneous because infrequent swimmer trajectories with a small radius of curvature R contribute strongly (as $1/R^3$) to the total flow. Active pattern formation also requires vertical symmetry breaking by sedimentation, which counters fluid incompressibility by effectively allowing nonmotile cells to cross streamlines, and permits them to deplete or accumulate in the downward or upward flow regions, respectively. The sedimentation biased fluid flow thus plays the role of an effective advection landscape for the nonmotile cells, which fluctuates on 10 s to 1 min timescales because of the slow rearrangements of the motile cells circles. This is sufficiently slow compared to nonmotile cell diffusion to allow density patterns to emerge, while also making them fluctuate and limiting their amplitude. Our results hence demonstrate that a purely physical mechanism exists for pattern formation in bacterial populations, which takes place over a wide range of physiologically relevant densities, where it notably enhances and reshapes aggregation of nonmotile cells when they express surface adhesins. We thus expect it to play an important role in the structuration of natural microbial communities.

Two control parameters that we identified experimentally materialize the two necessary elements for pattern formation. The nonmotile sedimentation inverse length $1/\lambda_{\mathrm{sed}} = v_{\mathrm{sed}}/D_{\mathrm{NM}}$ controls the level of nonmotile vertical asymmetry. We nondimensionalize it to h/λ_{sed} because, for patterns to occur, λ_{sed} needs to be smaller than the size of the recirculation loop, which is proportional to the channel height (Figs. 4 and 5; SM [66], Fig. S10). At high motile cell density, h/λ_{sed} decreases as the nonmotile effective diffusion coefficient increases, which explains the reduced heterogeneity level (SM, Figs. S7 and S11). With this exception, streamline crossing controlled by the tunable h/λ_{sed} is independent of the hydrodynamic interactions with the motile cells. Hence, self-organization in the binary mixture differs profoundly from self-assembly in purely active systems, where particle activity generates both of these aspects [72,73,80]. This decoupling could be exploited in the design of responsive materials to facilitate the control on self-assembly.

The second control parameter is the persistence time of the circular swimming τ, which is primarily controlled by the tumbling rate (Fig. 2), but also by tumbling angles and

rotational diffusion [18,20,22,23]. Their reduction for WT elongated cells [74] could explain the increased heterogeneity there (SM [66], Fig. S5). Interestingly, reduced tumbling [75] and possibly diffusion [23] at surfaces increase swimming persistence, which likely further reinforces the recirculative flows. We can define from τ a second nondimensional parameter, a Péclet number $\mathrm{Pe} = \langle v_{\mathrm{adv}} \rangle^2 \tau / D_{\mathrm{NM}}$, which compares advection by the swimmer-induced recirculation flows to diffusion. This number also accounts for the typical strength of the recirculation flows $\langle v_{\mathrm{adv}} \rangle$, which depends on the swimmers volume fraction, but also on the height of the channel, via its effect on the strength of hydrodynamic interactions [27]. In the $h = 20\,\mu\mathrm{m}$ channels, the disappearance of heterogeneities is thus likely due to a reduction of both h/λ_{sed} (from $\simeq 8$ to 3) and Pe (SM [66], Fig. S9).

Our model contains the minimal ingredients to capture all the experimental features well in simulations. However, we neglected not only steric interactions, but also hydrodynamics-driven collective sedimentation effects between nonmotile cells, which can produce heterogeneities by themselves [68,69]. These effects might reinforce the heterogeneities induced by motile cells, possibly explaining the somewhat lower heterogeneity level in simulations compared to experiments (Fig. 5).

The density patterns we uncovered form via a new type of collective structuration for bacteria. The mechanism for density pattern formation differs strongly from motility-induced phase separation (MIPS), the most studied physical self-organization mechanism for self-propelled active matter [29–33,55,56]. The spatial localization of the motile cells is indeed not affected (SM [66], Fig. S3) and their influence on the nonmotile cells can be explained only considering hydrodynamic interactions (Fig. 3), whereas MIPS is instead suppressed by them [76]. Our results thus highlight the importance of these interactions even below the onset of bacterial turbulence [24,26,27], where they are rarely accounted for. In the most heterogeneous mixtures, the fluid flows are not strong enough to visibly affect other swimmers, but a flow structure has already emerged, which is revealed by nonswimmers. This flow structure might nonetheless still have subtle effects on motile cells, e.g., on their chemotactic swimming [27].

Whereas active turbulence and other types of self-assembly in active swimmer populations result from interactions mediated by the instantaneous flow fields [72,73,77], interactions in the mixture feature a more complex temporal structure. Borrowing from previous theoretical works [78], we can indeed decompose the hydrodynamic interactions in instantaneous noise, which enhances diffusion, on top of a flow structure, which is only revealed by averaging over the typical duration of a circular revolution (few seconds), and which fluctuates on the timescale of circle rearrangements (tens of seconds). Our PIV measurements revealed both the spatial features [Fig. 3(b)] and the temporal persistence [Fig. 3(c)] of this flow structure. The temporally varying and space-structured flow field created by the swimmers, together with the gravity constraint, can thus be interpreted in terms of a temporally fluctuating advection landscape for the nonmotile bacteria. This is the basis for the emergence of fluctuation-dominated phase ordering (FDPO) on a fluctuating surface

[59–61], with which our system shares strongly similar characteristics, including giant number fluctuations of cell density and nonexponentially decaying correlation functions (SM [66], Fig. S1). This is surprising because, although mostly studied in theory and simulations, FDPO is a characteristic of active nematic systems, best materialized by active actin suspensions [60,61]. We find here that our bacterial system, which is more often thought of as polar active matter, provides an experimental realization of this idea.

Experiments with rapidly sedimenting or two-dimensionally constrained beads have shown that swimming bacteria can generate attractive interactions between them [45], which can lead to collective aggregation [46,47]. This behavior is purely two-dimensional and was mainly interpreted as an active depletion interaction effect. The shape of the fluid flow generated by surface swimmers may, however, contribute to it, in a low diffusion and infinite sedimentation limit of our system. The aggregative behavior we observe [Fig. 1(f)] is also similar to recently observed aggregation of sticky colloids in the presence of motile cells [79]. In contrast, the self-organization we observe differs strongly from the depletion at walls of colloids that are mixed under confinement with algal swimmers [57], which is unsurprising given the differences in the hydrodynamics of both systems. Other flagellated algae that swim in circles at surfaces, however, generate recirculative flow fields, which, though they differ quite strongly from the bacterial ones due to different body plans [80], might still drive similar density pattern emergence. Active particles attached to surfaces can affect local dynamics, a phenomenon coined active carpet [78], by enhancing diffusion and creating fluid transport [81,82], mostly observed in eukaryotic cells like in the synchronously beating cilia [83] but also in such prokaryotic systems as engineered surfaces covered with attached flagellated bacteria [84]. Our observations fit in this general framework, further highlighting the importance of micro-organism-surface interactions. However, in our case, the structure emerges from a population of freely swimming cells interacting with the surface.

We expect our results to be relevant to microbial community dynamics and structure in natural settings. A wide variety of communities might indeed be affected because the emergence of the patterns requires a relatively small fraction of motile cells, and the flow fields they generate are strong enough to also affect slowly moving microbial species (at speeds $\lesssim 1\,\mu m/s$). Recirculative flows generated by flagellated algae [80] suggest that similar pattern formation can happen in a wide variety of microbial communities. The fluctuating pattern formation plays a role in the enhancement of self-aggregation [Fig. 1(f)], and it could also influence the formation of biofilms in complex multispecies communities [64]. Further investigation should determine the precise consequences of the structures generated by motile cells on the environmental fitness of both species, but previous works notably suggest an enhanced protection against adverse conditions [35,64]. Additionally, while chemotaxis is not necessary for the emergence of the patterns, it is likely that chemical interactions modulate this behavior in more natural settings [35–39,62–64]. Finally, when coupled with self-aggregation behaviors and responses to physicochemical cues, we expect

the new route for pattern formation we uncovered to allow better understanding and thus harnessing of self-assembly in biological but also synthetic and microrobotic systems that attempt structuring for macrofabrication or biomedical purposes.

APPENDIX: METHODS

1. Strains and plasmids

All the strains and plasmids used in this study are listed in Table S1. All strains are derived from *Escherichia coli* wild-type strain W3110 (RpoS+) [85]. Except in the aggregative strain [Fig. 1(f)], the gene *flu*, which encodes for the major adhesin in our growth conditions (Antigen 43), was deleted in all strains to prevent cell aggregation [35]. Gene deletions are carried out using the plasmid pSIJ8 [86], by lambda Red recombination (0.15% arabinose induction) with a Kanamycin (Kan) resistance cassette, which is then removed with flippase recombinase (50 mM L-rhamnose induction). The plasmid pSIJ8 is then removed by growth at 42 °C. The nonmotile strains lack the flagellin FliC, the nontumbling strain the chemotaxis response regulator CheY, and the tumbling-only strain the phosphatase CheZ.

All strains are fluorescently labeled with fluorescent proteins mCherry or mNeonGreen expressed from a plasmid with pTRc99a backbone [87] with a strong ribosome binding site (RBS2) [88]. Motile strains were usually tagged with mCherry and nonmotile strains with mNeonGreen. Reversing the tags gave identical results [SM [66], Fig. S1(c)]. The growth medium is supplied with 100 μM Isopropyl β-d-1-thiogalactopyranoside (IPTG) for fluorescent protein expression induction and 0.1 mg/mL Ampicillin as antibiotic resistance marker. The nonchemotactic but tumbling strain expresses $cheY^{D13K,Y106W}$ ($cheY$**) from a plasmid with pTRc99a backbone transformed in the $\Delta cheY$ strain. No IPTG was added; the expression of CheY** resulted only from the leaky expression of the plasmid. At this expression level, the tumbling rate is similar to WT [35]. This strain was tagged with mCherry expressed from pOSK237, a plasmid with pBAD backbone, adding 0.004% L-arabinose for protein induction and 50 μg/mL Kanamycin as an antibiotic resistance marker in the growth medium. In the adhesive nonmotile strain ($flu+$, $\Delta fliC$), the normally phase-variable chromosomal expression of Antigen 43 was locked to the ON state by overexpressing the Dam methyltransferase from the leaky expression ([IPTG] = 0 μM) of a pTRc99a-*dam* plasmid, following previous protocol [35]. This strain was tagged with EGFP expressed from pOSK239, a plasmid with pBAD backbone, adding 0.004% L-arabinose for protein induction

and 50 µg/mL Kanamycin as antibiotic resistance marker in the growth medium.

2. Experimental chamber microfabrication

Molds were fabricated using standard photolithography and microfabrication techniques. The SU8 photoresist (Microchem^{TM}) was spin-coated on a silicone wafer, prebaked, shaped by patterned UV exposure, postbaked, and washed according to manufacturer instructions. The cast was then passivated with silane and checked using a profilometer. Poly-di-methylsiloxane (PDMS) was poured on the cast in a 1:10 crosslinker to base ratio, degassed, baked overnight at 65 °C, peeled off, cut to shape, and covalently bound on isopropanol-rinsed microscopy high-precision glass slides after oxygen plasma treatment. PDMS to glass covalent bonds were allowed to form for 20 min at room temperature, and the devices were then filled with the samples.

3. Phase diagram assays

a. Cell growth and sample preparation

Cells are grown overnight in liquid tryptone broth (TB) medium (1% Bacto tryptone + 0.5% NaCl) with appropriate antibiotics at 37 °C. The overnight culture is diluted 1/100 in 10 mL fresh TB supplemented with antibiotics and inducers and grown at 34 °C under shaking at 270 rpm for about 4 h, until the optical density at 600 nm of the suspension reached $OD_{600} \simeq 0.5$. For elongated cells, 100 µg/mL of cephalexin, which blocks cell division, is added 60 min (i.e., about 1.5 cell cycles) before harvesting the cells, yielding about two to four times longer cells than without treatment. The whole culture is then centrifuged at 3.5 krpm for 5 min to prevent any damage to the flagella of motile cells. The pellet is resuspended in motility buffer (MB) (10 mM KPO$_4$ + 0.1 mM EDTA + 67 mM NaCl + 0.01% Tween 80, pH=7.0) + 1% Glucose. This buffer allows cells to swim but not to grow. Tween 80 is a surfactant that prevents cell-surface adhesion [89].

Cells are brought to a high density ($OD_{600} = 60$) by a subsequent centrifugation (3.5 krpm, 5 min). Six serial dilutions in MB are done for each strain. Each dilution of a strain is mixed with a dilution of the other in a 1:1 ratio, yielding 36 binary mixtures. Each mixture is then loaded in a previously fabricated straight microfluidic channel of 1 cm length, 1 mm width, and 50 µm height, if not indicated otherwise. The channel is then sealed with grease to prevent fluid flows. For steady-state measurements, images are acquired after letting the mixtures settle in the microfluidic device for at least 40 min. For time-dependent measurements, only two channels are filled at the same time, and brought immediately under the microscope. Each condition was probed in at least three independent biological replicates.

b. Passive particles

Control experiments with passive colloidal particles followed the same protocol as above, substituting nonmotile cells with FluoGreen-tagged PMMA particles from microParticles GmbH [90], with a 1.33 µm diameter and 1.19 g/cm^3 density. They are suspended in motility buffer to a final volume fraction of 2%.

c. Physically modified media

When varying the buoyancy of the medium, cells are grown and processed as described above, except that the last pellet resuspension and the serial dilutions are made in density-matching motility buffer. The latter is prepared using iodixanol to increase the MB density up to the same density as *E. coli* cells (1.11 g/mL). Iodixanol is a nonionic, noncytotoxic iodine compound that is commonly used as a density-matching agent and density gradient medium. It has little effect on the suspension's viscosity and is metabolically inert to *E. coli*. The density-matching motility buffer contains 26.6% iodixanol, the concentration of the other components being unchanged. For the experiments with different buoyancies, the volume fractions of iodixanol were 0% ($\Delta \rho g = 1$), 13.2% ($\Delta \rho g = 0.5$), 19.9% ($\Delta \rho g = 0.25$), 23.9% ($\Delta \rho g = 0.1$), 26.6% ($\Delta \rho g = 0$).

4. Epifluorescence microscopy

The density fluctuations are visualized using the Nikon Ti-E inverted fluorescence widefield microscope with a 20× (NA 0.75) objective and the mCherry (excitation filter 572/25, emission 645/90) and GFP (excitation filter 470/40, emission 525/50) filters. Images are acquired in the focal plane 8 µm above the bottom of the microfluidic channel. Focal plane is maintained using the Nikon perfect focus system.

a. Density fluctuations quantification

A stack of images of nine different positions spanning across the microfluidic channel is acquired seven times for each fluorescence channel with the Andor Zyla sCMOS camera and NIS software (1 px = 0.32 µm, field of view = 2048×2048 px^2, 50 ms exposure). Further image processing is realized with Fiji [91]. Each image in the stack is corrected for inhomogeneous illumination. For this, an illumination background image is computed at each cell density as the median fluorescence of a large set of images taken at this density. The intensity of this background image is then normalized by its mean. Each image of the stack is divided by the illumination background image corresponding to its cell density. To further correct for small remaining systematic biases in the intensity profile of each image, a quadratic polynomial filter is applied.

The spatial autocorrelation function of the corrected intensity is computed as

$$C(\mathbf{r}) = \frac{1}{n(\mathbf{r})} \sum_{\mathbf{r_0}}^{n(\mathbf{r})} \left(\frac{I(\mathbf{r} + \mathbf{r_0})I(\mathbf{r_0})}{\langle I^2 \rangle} - 1 \right), \qquad (A1)$$

where $n(\mathbf{r})$ is the number of valid initial pixel positions $\mathbf{r_0}$ for a given spatial shift $\mathbf{r}$. In homogeneous control, this function decays over a length scale of about 1 µm corresponding to the bacterial size, whereas a second decay appears at several tens of microns when density fluctuations are present [SM [66], Fig. S1(e)].

The density fluctuations are quantified by calculating the heterogeneity level of the images. For this, each image is divided into nonoverlapping squares of size N, allowed to vary from $N = (2^0)^2$ px^2 to $N = (2^9)^2$ px^2 [SM [66], Fig. S1(a)].

The sum of the fluorescence intensity $I_{\mathbf{k},N} = \sum_{\mathbf{j}}^{N} I_{\mathbf{k}+\mathbf{j}}$ is computed within each square (indexed by $\mathbf{k}$). The spatial variance σ_N^2 of this total intensity is then computed across the squares of size N,

$$\sigma_N^2 = \mathrm{var}_{\mathbf{k}}(I_{\mathbf{k},N}). \tag{A2}$$

The latter is then normalized by the pixel size of the slice (N) and by the variance over squares of size $N = 1$, σ_1^2 [SM [66], Fig. S1(b)], since one expects from the central limit theorem that $\sigma_N^2 = N\sigma_1^2$ for an image made of pixels that assume random noncorrelated values. The ratio $\sigma_N^2/N\sigma_1^2$ increasing as a power of N then marks large-scale correlations in the spatial distribution of fluorescence intensity, often called giant number fluctuations [93].

Since our images have a texture that comes from the cells being several pixels large, even in homogeneous samples, $\sigma_N^2/N\sigma_1^2$ transiently increases with N until the latter reaches the area of a single cell ($N \sim 100$ px^2), above which $\sigma_N^2/N\sigma_1^2$ becomes constant as a function of N. In contrast, in samples with density fluctuations, $\sigma_N^2/N\sigma_1^2$ keeps increasing for $N > 100$ px^2, marking the large-scale fluctuations of the cell density [SM [66], Fig. S1(b)]. To reduce the corresponding heterogeneity level to a single number, we use $\sigma_N^2/N\sigma_1^2$ for a square of area $N = (2^7)^2$ px^2 = 16 384 px^2. The width of this square is indeed about 42 μm, which corresponds to the large-scale decay of the spatial autocorrelation function of the pixel intensity [SM [66], Fig. S1(e)]. Since the value of $\sigma_N^2/N\sigma_1^2$ for $N = (2^7)^2$ in the control passive systems varies little across nonmotile volume fractions and is close to 400 on average, we further defined the heterogeneity level as $(\sigma_N^2/N\sigma_1^2)/400$ for $N = (2^7)^2$, such that passive systems have a heterogeneity level of 1 on average, and heterogeneity is defined relative to this homogeneous case.

b. Image velocimetry analysis

A movie of 7500 binned frames is acquired at 5 frames per second with the Andor Zyla sCMOS Camera and NIS software (1 px = 1.3 μm, field of view = 512×512 px^2, 50 ms exposure). The velocity field, the flow structure factor, and the kinetic energy of the nonmotile cells are measured using a local image velocimetry algorithm based on Fourier image analysis, following previously described protocol [27] (code at [92]). In short, local instantaneous displacements are computed on a rectangular grid with 4 px spacing, using Gaussian-filtered (half-width 3 px) squared subframes (32×32 px^2). Local velocities are then fitted from cumulative displacements on either a 10-frames-long sliding window [Figs. 3(a) and 3(b) and SM [66], Fig. S6], or a 2 frames sliding window, to improve temporal resolution at the expense of an increased measurement noise, in the case of Fig. 3(d). The spatial Fourier transform of the velocity field is computed as

$$\mathbf{v}(\mathbf{q}, t) = \sum_{\mathbf{x}} \mathbf{v}(\mathbf{x}, t) \exp\left(-i\mathbf{q} \cdot \mathbf{x}\right), \tag{A3}$$

the power spectrum as

$$E(q) = q\langle|\mathbf{v}(\mathbf{q}, t)|^2\rangle_{|\mathbf{q}|=q,t} / \langle|\mathbf{v}(\mathbf{x}, t)|^2\rangle_{|\mathbf{x}|,t}, \tag{A4}$$

and the time autocorrelation function as

$$C_v(t; q) = \frac{\langle\mathbf{v}(\mathbf{q}, t + t_0)\mathbf{v}(\mathbf{q}, t_0)\rangle_{|\mathbf{q}|=q,t_0}}{\langle|\mathbf{v}(\mathbf{q}, t)|^2\rangle_{|\mathbf{q}|=q,t}}. \tag{A5}$$

5. Confocal microscopy

The binary mixtures are prepared following the above-mentioned sample preparation and are visualized using a Zeiss LSM-880 confocal microscope equipped with a C-Apochromat 40× (NA 1.2) water immersion objective. Motile cells (tagged with mCherry) and nonmotile cells (tagged with mNeonGreen) are visualized using the 594 nm helium-neon laser and 488 nm argon laser, and detected with a photomultiplier at 490–535 and 598–660 nm, respectively.

a. Cell fraction vertical distribution

Z-stack images of the whole microfluidic channel are acquired using the ZEN Black software (Zeiss) (1 px = 0.2 μm in X and Y, 1 μm in Z; field of view = 303.64×303.64×70 μm^3; 0.35 μs/px exposure). The number of cells in each Z plane is quantified by the connected components labeling algorithm for ImageJ [94]. Because the height and the tilt of the microfluidic channels vary slightly from sample to sample ($<10\%$), the Z position is binned and the mean of the cell fraction over the bins is calculated. The sedimentation length λ_{sed} is extracted by fitting an exponential decay, $Ae^{-z/\lambda_{\mathrm{sed}}}$, to the vertical density profiles.

b. 3D tracking

To track the horizontal and vertical motion of the non-motile cells, the binary mixtures are prepared following the above-mentioned sample preparation. To be able to track single nonmotile cells, only 0.03% of them are fluorescently labeled. Low-density regions ("holes") of the mixtures are identified with transmitted light, and Z-stacks are acquired at the highest possible speed around these regions using the ZEN Black software (Zeiss) (1 px = 0.54 μm in X and Y, 2 μm in Z; field of view = 163.5×163.5×20 μm^3; 1.3 μs/px exposure; ~0.3 fps).

The three-dimensional trajectories are reconstructed using the Mosaic plugin (MosaicSuite-1.0.1) for ImageJ [95]. From each trajectory is then extracted their relative position to the hole center (defined by transmitted light) and their velocities in the vertical and horizontal planes.

6. Motility assay and circular trajectories measurements

From an overnight culture, cells are grown in TB for 4 h at 34 °C. The culture is centrifuged (3.5 krpm for 5 min), and the pellet is resuspended twice, first in MB + 1% glucose and then in the adequate buffer (MB, MB + 26.6% iodixanol). The sample is then loaded in a previously fabricated microfluidic channel.

Cell motility is recorded with a Nikon TI microscope at 10× (NA 0.3) magnification. A stack of 10 000 frames at 100 frames per second is acquired under phase contrast illumination with an Eosens 4cxp CMOS camera and StreamPix Multicamera software. The swimming speed of cells, the fraction of motile cells, and the diffusion coefficient of

nonmotile cells (SM [66], Fig. S7) are measured using differential dynamic microscopy [96] following previously described protocol [27].

To reconstruct the horizontal trajectories of the cells close to the surface, a stack of 2000 frames at 50 frames per second is acquired. Single 2D trajectories are reconstructed using the plugin ParticleTracking for ImageJ (code at [97]). Cell trajectories are categorized into runs and tumbles as previously described [98]. To calculate the radius of curvature of the trajectories, only runs are considered. The parametric curvature $C(t)$ is calculated for frame t as

$$C(t) = \left| \frac{(\dot{x}^2 + \dot{y}^2)^{\frac{3}{2}}}{(\dot{x}\ddot{y} - \ddot{x}\dot{y})} \right|, \tag{A6}$$

where the first and second derivatives of $x(t)$ and $y(t)$ are extracted from the cell tracking data by Taylor expansion. For this, a 50 frame sliding window is considered around time t, over which $x(t')$ and $y(t')$ are least-squares fitted to a second-order polynomial to obtain their first and second derivatives, as given by Taylor's expansion:

$$f(t') = \sum_{n=0}^{2} f^{(n)}(t) \frac{(t' - t)^n}{n!} + O((t' - t)^3). \tag{A7}$$

The mean curvature is computed for each run, and for each trajectory as the average of $C(t)$ over all times t for which the cell is categorized as running. The radius is then the inverse of the curvature, $R = 1/\langle C(t) \rangle$. When computing histograms of the mean radius R, each trajectory has a weight equal to its duration.

To estimate the circle persistence time of a trajectory of duration T, we compute the mean linear displacement

$$dr(t) = \langle \sqrt{[\Delta x(t, t_0)]^2 + [\Delta y(t, t_0)]^2} \rangle_{t_0 \in [1, T-t]} \tag{A8}$$

with $\Delta x(t, t_0) = x(t + t_0) - x(t_0)$, and we find the smallest lag time $t = \tau$ for which $dr(t)$ exceeds the distance $3R$, with R the above-defined radius of curvature, i.e., 1.5 times the average circle diameter. If $dr(t)$ never exceeds $3R$, we assign $\tau = T$.

7. Numerical simulations

All simulations were performed in a three-dimensional rectangular box of width and length W and of height H. Boundary conditions are periodic on the lateral edges of the simulation box, and reflexive no-slip at the top and bottom walls. Cell volume fractions are $\phi = nV/HW^2$, with n the number of cells, and the cell volume V being twice as high for elongated cells. All parameter values are given in Table S2.

a. Mean flow field generated by a circular swimmer

The motile cell is modeled as a pusher dipole of point forces, representing the cell body and the flagellum, both of magnitude $f_0/6\pi\eta = a^S v_0$, with η the fluid viscosity, a^S the hydrodynamic radius of the cell body, and v_0 the swimming speed [15]. The fluid flow $\mathbf{v}^{i \leftarrow j}$ in position $\mathbf{x}_i$ generated by a point force $\mathbf{f}_j$ positioned in $\mathbf{x}_j$ is

$$\mathbf{v}^{i \leftarrow j} = \mathbf{\Omega}^{i \neq j} \cdot \frac{\mathbf{f}_j}{6\pi\eta}, \tag{A9}$$

where $\mathbf{\Omega}^{i \neq j}$ is the normalized hydrodynamic-interaction tensor, i.e., the normalized Green function, in our geometry, of the incompressible Stokes equation:

$$-\nabla p + \eta \Delta \mathbf{v} + \mathbf{f} = \mathbf{0}, \tag{A10}$$

$$\nabla \cdot \mathbf{v} = \mathbf{0}. \tag{A11}$$

The tensor $\mathbf{\Omega}^{i \neq j}$ and therefore the hydrodynamic flows $\mathbf{v}^{i \leftarrow j}$ are computed using the two-dimensional Fourier-space expansion of the hydrodynamic flow introduced in Mucha *et al.* [70], using the $N \log(N)$ algorithm of Hernandez-Ortiz *et al.* [71]. It allows an efficient calculation of the fluid flow generated by multiple point forces in our geometry via the additivity of the solutions to the Stokes equation (SM [66], notes). The dipole flow $v^D(\mathbf{x}; \mathbf{x}_0, \mathbf{u})$ is the sum of the flow generated by the two point forces, $+\mathbf{u} f_0$ located at $\mathbf{x}_0 + l_d \mathbf{u}$ (cell body), and $-f_0 \mathbf{u}$ located at $\mathbf{x}_0 - l_d \mathbf{u}$ (flagellum), with $\mathbf{x}_0$ the position of the center of the cell, $\mathbf{u}$ the unit vector pointing in the swimming direction, and l_d the half dipole length. To describe circular surface swimmers, the dipoles are horizontal and located at a height $z_M = 0.7$ μm from the surface over which they circulate. The mean flow field generated over one revolution is computed as the average of the dipole flow:

$$v_{1r}(\mathbf{x}; R) = \frac{1}{n\theta} \sum_{k=0}^{n\theta-1} v^D(\mathbf{x}; \mathbf{x}_k, \mathbf{u}_k) \tag{A12}$$

over $n\theta = 100$ equally spaced positions of the dipole on a circle of radius R, $\mathbf{x}_k = (R \cos\theta_k, R \sin\theta_k, z_M)$, with $\theta_k = 2\pi k/n\theta$, the dipole being tangential to the circle, $\mathbf{u}_k = (-\sin\theta_k, \cos\theta_k, 0)$. Because this configuration of forces is rotationally symmetric, the mean flow field only depends on the longitudinal (z) and radial (r) coordinates in the cylindrical coordinate system relative to the center of the circle, and has no azimuthal component.

The flow field was analyzed using MATLAB (version 2020a). We define the inward flux generated by the circular swimmer at a distance r by

$$\Phi(r) = 2\pi r \int_0^H |\mathbf{v}_{1r}(r, z \,|\, \mathbf{v}_{1r} \cdot \mathbf{u}_r < 0) \cdot \mathbf{u}_r| \, dz \tag{A13}$$

with $\mathbf{u}_r$ the radial unit vector. The recirculation radius is defined as the distance r which maximizes Φ, corresponding to the position of the center of the recirculation whirl. The recirculation flux is defined as the maximal flux $\max_r \Phi(r)$.

The vertically averaged $v_{1r}(\mathbf{x}; R)$ of Figs. 3(e) and 3(f) is computed as

$$\langle v \rangle(r) = \int_0^{Hc} dz \, v_{1r}((r, z); R) p(z), \tag{A14}$$

with the fitted tracer distribution

$$p(z) = \frac{\exp(-z/\lambda_{\text{sed}})/\lambda_{\text{sed}}}{\int_0^{Hc} dz \exp(-z/\lambda_{\text{sed}})}, \tag{A15}$$

$\lambda_{\text{sed}} = 10$ μm is the experimental decay length, and $Hc = 20$ μm is the height of the acquisition volume.

b. Distribution of tracers in the mean flow field of a population of circular swimmers

A population of n_{Mc} [250–(5×10^4)] circular swimmers is simulated. They are assigned with equal probability to the top ($z = H - z_M$) or bottom ($z = z_M$) wall, mimicking experiments [SM [66], Fig. S7(b)]. The centers of the circles are distributed uniformly in the horizontal (x, y) directions. The circle radius is drawn from a double log normal distribution

$$p(R) = f g(\log R, m_1, s_1) + (1 - f) g(\log R, m_2, s_2), \quad \text{(A16)}$$

with

$$g(x, m, s) = \exp\left(-(x - m)^2/(2s^2)\right)/\sqrt{2\pi s^2}, \quad \text{(A17)}$$

and $\log R$ is the basis 10 logarithm of the radius expressed in µm. The distribution was parametrized to fit the experimental distribution of circle radii for normal-sized and elongated cells [SM [66], Fig. S11(a)]. We perform a simplified Brownian dynamics simulation of the motion of n_{NM} [(5×10^3)–(2×10^4)] nonmotile cells that are subjected to the total mean flow field generated by the circles, gravity, and Brownian motion. The evolution of the 3D position of tracer i obeys

$$d\mathbf{r}_i = \left[\mathbf{v}_{\text{sed}} + \sum_{j}^{\text{dipoles}} v_{1r}(\mathbf{r}_i - \mathbf{x}_j; R_j)\right] dt + \sqrt{2D_{\text{NM}}}\, d\mathbf{w}_i \quad \text{(A18)}$$

with $\mathbf{v}_{\text{sed}}$ the downward-oriented sedimentation speed, $\mathbf{x}_j$ and R_j the center and radius of circle j, which are kept fixed throughout the simulation, dt the simulation time step, D_{NM} the diffusion coefficient of the nonmotile cells, and $d\mathbf{w}_i = \sqrt{dt}\sigma_i$ the normalized Brownian noise. The Gaussian-distributed three-dimensional random variable σ_i has unit variance and no cross-correlation with $\sigma_{j \neq i}$. The initial distribution of nonmotile cells is uniform horizontally and obeys the Boltzmann distribution in confined geometry along the vertical axis

$$p(z_i, t = 0) = \frac{v_{\text{sed}}}{D_{\text{NM}}} \frac{\exp(-z_i v_{\text{sed}}/D_{\text{NM}})}{1 - \exp(-H v_{\text{sed}}/D_{\text{NM}})}. \quad \text{(A19)}$$

Steric interactions, direct hydrodynamic interactions between nonswimmers, and the effect of confinement on self-diffusion are neglected (SM [66], notes). The equation of motion is time-integrated using an Euler scheme, with $dt = 0.1$ s in equivalent real time. The configuration of the system is saved every step, for a total duration of the simulation of 1000 steps. Because the circle configuration and thus the velocity field are fixed, the time elapsed since the beginning of the simulation can be interpreted as a persistence time of the circles, and the configuration after this time as a realization of the structure of the population of nonmotile cells in the mixture for said persistence time.

A pseudoimage of the suspension is produced for each simulation time step from the positions of the nonmotile tracers. It renders the microscopy image that is expected under our experimental conditions for the given nonmotile cells configuration, assuming a Gaussian point spread function for our objective. Each particle, positioned in ($\mathbf{r}_i = (x_i, y_i), z_i$), contributes to the intensity in position $\mathbf{r} = (x, y)$ in the rendered image at $h_0 = 8$ µm above the bottom of the channel as

$$I_i = \frac{1}{1 + 3s^2} \exp\left(\frac{2(\mathbf{r} - \mathbf{r}_i)^2}{a_d^2(1 + 3s^2)}\right), \quad \text{(A20)}$$

with $s = (z_i - h_0)/dh$ the distance to the focal plane, normalized to the depth of field dh. The images are printed with a pixel size of $\text{px}_{\text{sim}} = 1$ µm, which is larger than in our experimental setup, to save computer memory. They are then analyzed with the same algorithms as the experimental data. We used a box size of 32×32 µm^2 to compute the heterogeneity level as $\sigma_N^2/N\sigma_1^2$, averaged over the persistence time window [500, 700] steps, and normalized to its value in the purely passive homogeneous control similarly to experiments. The value of $\sigma_N^2/N\sigma_1^2$ in the simulated passive system is 8.9, smaller than in experiments, as expected due to the smaller pixel size there (1 $\text{px}_{\text{exp}} = 0.325$ µm).

The simulations for each parameter set are repeated six times, and quantifications are averaged over these repeats. This relatively small number of repeats is sufficient because the heterogeneity level varies little between independent repeats. The fully parallelized java code for running the simulations is available on Github [99] and GitLab [100].

[1] O. X. Cordero and M. S. Datta, Microbial interactions and community assembly at microscales, Curr. Opin. Microbiol. **31**, 227 (2016).

[2] C. D. Nadell, K. Drescher, and K. R. Foster, Spatial structure, cooperation and competition in biofilms, Nat. Rev. Microbiol. **14**, 589 (2016).

[3] S. Azimi, G. R. Lewin, and M. Whiteley, The biogeography of infection revisited, Nat. Rev. Microbiol. **20**, 579 (2022).

[4] S. Lion and M. Baalen, Self-structuring in spatial evolutionary ecology, Ecol. Lett. **11**, 277 (2008).

[5] W. Liu, H. L. Røder, J. S. Madsen, T. Bjarnsholt, S. J. Sørensen, and M. Burmølle, Interspecific bacterial interactions are reflected in multispecies biofilm spatial organization, Front. Microbiol. **7**, 1366 (2016).

[6] D. Yanni, P. Marquez-Zacarias, P. J. Yunker, and W. C. Ratcliff, Drivers of spatial structure in social microbial communities, Curr. Biol. **29**, R545 (2019).

[7] L. Eigentler, F. A. Davidson, and N. R. Stanley-Wall, Mechanisms driving spatial distribution of residents in colony biofilms: An interdisciplinary perspective, Open Biol. **12**, 220194 (2022).

[8] H. C. Berg and R. A. Anderson, Bacteria swim by rotating their flagellar filaments, Nature (London) **245**, 380 (1973).

[9] Y. Tu, Quantitative modeling of bacterial chemotaxis: Signal amplification and accurate adaptation, Annu. Rev. Biophys. **42**, 337 (2013).

[10] R. Colin and V. Sourjik, Emergent properties of bacterial chemotaxis pathway, Curr. Opin. Microbiol. **39**, 24 (2017).

[11] A. J. Waite, N. W. Frankel, and T. Emonet, Behavioral variability and phenotypic diversity in bacterial chemotaxis, Annu. Rev. Biophys. **47**, 595 (2018).

[12] R. Colin, B. Ni, L. Laganenka, and V. Sourjik, Multiple functions of flagellar motility and chemotaxis in bacterial physiology, FEMS Microbiol. Rev. **45**, fuab038 (2021).

[13] M. E. Cates, Diffusive transport without detailed balance in motile bacteria: Does microbiology need statistical physics? Rep. Prog. Phys. **75**, 042601 (2012).

[14] K. Drescher, J. Dunkel, L. H. Cisneros, S. Ganguly, and R. E. Goldstein, Fluid dynamics and noise in bacterial cell-cell and cell-surface scattering, Proc. Natl. Acad. Sci. USA **108**, 10940 (2011).

[15] J. Elgeti, R. G. Winkler, and G. Gompper, Physics of microswimmers–single particle motion and collective behavior: A review, Rep. Prog. Phys. **78**, 056601 (2015).

[16] M. A.-S. Vigeant, R. M. Ford, M. Wagner, and L. K. Tamm, Reversible and irreversible adhesion of motile *Escherichia coli* cells analyzed by total internal reflection aqueous fluorescence microscopy, Appl. Environ. Microbiol. **68**, 2794 (2002).

[17] A. P. Berke, L. Turner, H. C. Berg, and E. Lauga, Hydrodynamic attraction of swimming microorganisms by surfaces, Phys. Rev. Lett. **101**, 038102 (2008).

[18] G. Li and J. X. Tang, Accumulation of microswimmers near a surface mediated by collision and rotational Brownian motion, Phys. Rev. Lett. **103**, 078101 (2009).

[19] S. Bianchi, F. Saglimbeni, and R. Di Leonardo, Holographic imaging reveals the mechanism of wall entrapment in swimming bacteria, Phys. Rev. X **7**, 011010 (2017).

[20] G. Junot, T. Darnige, A. Lindner, V. A. Martinez, J. Arlt, A. Dawson, W. C. K. Poon, H. Auradou, and E. Clement, Run-to-tumble variability controls the surface residence times of *E. coli* bacteria, Phys. Rev. Lett. **128**, 248101 (2022).

[21] E. Lauga, W. R. DiLuzio, G. M. Whitesides, and H. A. Stone, Swimming in Circles: Motion of bacteria near solid boundaries, Biophys. J. **90**, 400 (2006).

[22] G. L. Li, L. K. Tam, and J. X. Tang, Amplified effect of Brownian motion in bacterial near-surface swimming, Proc. Natl. Acad. Sci. USA **105**, 18355 (2008).

[23] E. Perez Ipiña, S. Otte, R. Pontier-Bres, D. Czerucka, and F. Peruani, Bacteria display optimal transport near surfaces, Nat. Phys. **15**, 610 (2019).

[24] A. Sokolov, I. S. Aranson, J. O. Kessler, and R. E. Goldstein, Concentration dependence of the collective dynamics of swimming bacteria, Phys. Rev. Lett. **98**, 158102 (2007).

[25] F. Ginelli, F. Peruani, M. Bär, and H. Chaté, Large-scale collective properties of self-propelled rods, Phys. Rev. Lett. **104**, 184502 (2010).

[26] H. H. Wensink, J. Dunkel, S. Heidenreich, K. Drescher, R. E. Goldstein, H. Löwen, and J. M. Yeomans, Meso-scale turbulence in living fluids, Proc. Natl. Acad. Sci. USA **109**, 14308 (2012).

[27] R. Colin, K. Drescher, and V. Sourjik, Chemotactic behaviour of *Escherichia coli* at high cell density, Nat. Commun. **10**, 5329 (2019).

[28] V. A. Martinez, E. Clement, J. Arlt, C. Douarche, A. Dawson, J. Schwarz-Linek, A. K. Creppy, V. Skultety, A. N. Morozov, H. Auradou, and W. C. K. Poon, A combined rheometry and imaging study of viscosity reduction in bacterial suspensions, Proc. Natl. Acad. Sci. USA **117**, 2326 (2020).

[29] M. E. Cates, D. Marenduzzo, I. Pagonabarraga, and J. Tailleur, Arrested phase separation in reproducing bacteria creates a generic route to pattern formation, Proc. Natl. Acad. Sci. USA **107**, 11715 (2010).

[30] Y. Fily and M. C. Marchetti, Athermal phase separation of self-propelled particles with no alignment, Phys. Rev. Lett. **108**, 235702 (2012).

[31] M. E. Cates and J. Tailleur, Motility-induced phase separation, Annu. Rev. Condens. Matter Phys. **6**, 219 (2015).

[32] I. Buttinoni, J. Bialke, F. Kummel, H. Löwen, C. Bechinger, and T. Speck, Dynamical clustering and phase separation in suspensions of self-propelled colloidal particles, Phys. Rev. Lett. **110**, 238301 (2013).

[33] C. Liu, X. Fu, L. Liu, X. Ren, C. K. Chau, S. Li, L. Xiang, H. Zeng, G. Chen, L. H. Tang, P. Lenz, X. Cui, W. Huang, T. Hwa, and J. D. Huang, Sequential establishment of stripe patterns in an expanding cell population, Science **334**, 238 (2011).

[34] J. Agudo-Canalejo and R. Golestanian, Active phase separation in mixtures of chemically interacting particles, Phys. Rev. Lett. **123**, 018101 (2019).

[35] L. Laganenka, R. Colin, and V. Sourjik, Chemotaxis towards autoinducer 2 mediates autoaggregation in *Escherichia coli*, Nat. Commun. **7**, 12984 (2016).

[36] E. O. Budrene and H. C. Berg, Dynamics of formation of symmetrical patterns by chemotactic bacteria, Nature (London) **376**, 49 (1995).

[37] S. Park, P. M. Wolanin, E. A. Yuzbashyan, H. Lin, N. C. Darnton, J. B. Stock, P. Silberzan, and R. Austin, Influence of topology on bacterial social interaction, Proc. Natl. Acad. Sci. USA **100**, 13910 (2003).

[38] J. Saragosti, V. Calvez, N. Bournaveas, B. Perthame, A. Buguin, and P. Silberzan, Directional persistence of chemotactic bacteria in a traveling concentration wave, Proc. Natl. Acad. Sci. USA **108**, 16235 (2011).

[39] X. Fu, S. Kato, J. Long, H. H. Mattingly, C. He, D. C. Vural, S. W. Zucker, and T. Emonet, Spatial self-organization resolves conflicts between individuality and collective migration, Nat. Commun. **9**, 2177 (2018).

[40] X.-L. Wu and A. Libchaber, Particle diffusion in a quasi-two-dimensional bacterial bath, Phys. Rev. Lett. **84**, 3017 (2000).

[41] M. J. Kim and K. S. Breuer, Enhanced diffusion due to motile bacteria, Phys. Fluids **16**, L78 (2004).

[42] Y. Peng, L. Lai, Y.-S. Tai, K. Zhang, X. Xu, and X. Cheng, Diffusion of ellipsoids in bacterial suspensions, Phys. Rev. Lett. **116**, 068303 (2016).

[43] R. Jeanneret, D. O. Pushkin, V. Kantsler, and M. Polin, Entrainment dominates the interaction of microalgae with micron-sized objects, Nat. Commun. **7**, 12518 (2016).

[44] J. Singh, A. E. Patteson, B. O. T. Maldonado, P. K. Purohit, and P. E. Arratia, Bacterial activity hinders particle sedimentation, Soft Matter **17**, 4151 (2021).

[45] L. Angelani, C. Maggi, M. L. Bernardini, A. Rizzo, and R. Di Leonardo, Effective interactions between colloidal particles suspended in a bath of swimming cells, Phys. Rev. Lett. **107**, 138302 (2011).

[46] S. Gokhale, J. Li, A. Solon, J. Gore, and N. Fakhri, Dynamic clustering of passive colloids in dense suspensions of motile bacteria, Phys. Rev. E **105**, 054605 (2022).

[47] J. Bouvard, F. Moisy, and H. Auradou, Ostwald-like ripening in the two-dimensional clustering of passive particles induced by swimming bacteria, Phys. Rev. E **107**, 044607 (2023).

[48] S. C. Takatori and J. F. Brady, A theory for the phase behavior of mixtures of active particles, Soft Matter **11**, 7920 (2015).

[49] F. Kümmel, P. Shabestari, C. Lozano, G. Volpe, and C. Bechinger, Formation, compression and surface melting of colloidal clusters by active particles, Soft Matter **11**, 6187 (2015).

[50] J. Stenhammar, R. Wittkowski, D. Marenduzzo, and M. E. Cates, Activity-induced phase separation and self-assembly in mixtures of active and passive particles, Phys. Rev. Lett. **114**, 018301 (2015).

[51] A. Wysocki, R. G. Winkler, and G. Gompper, Propagating interfaces in mixtures of active and passive Brownian particles, New J. Phys. **18**, 123030 (2016).

[52] P. Dolai, A. Simha, and S. Mishra, Phase separation in binary mixtures of active and passive particles, Soft Matter **14**, 6137 (2018).

[53] D. R. Rodriguez, F. Alarcon, R. Martinez, J. Ramírez, and C. Valeriani, Phase behaviour and dynamical features of a two-dimensional binary mixture of active/passive spherical particles, Soft Matter **16**, 1162 (2020).

[54] R. S. McCandlish, A. Baskaran, and M. F. Hagan, Spontaneous segregation of self-propelled particles with different motilities, Soft Matter **8**, 2527 (2012).

[55] R. Wittkowski, J. Stenhammar, and M. E. Cates, Nonequilibrium dynamics of mixtures of active and passive colloidal particles, New J. Phys. **19**, 105003 (2017).

[56] S. N. Weber, C. A. Weber, and E. Frey, Binary mixtures of particles with different diffusivities demix, Phys. Rev. Lett. **116**, 058301 (2016).

[57] S. Williams, R. Jeanneret, I. Tuval, and M. Polin, Confinement-induced accumulation and de-mixing of microscopic active-passive mixtures, Nat. Commun. **13**, 4776 (2022).

[58] M. C. Marchetti, J. F. Joanny, S. Ramaswamy, T. B. Liverpool, J. Prost, M. Rao, and R. A. Simha, Hydrodynamics of soft active matter, Rev. Mod. Phys. **85**, 1143 (2013).

[59] D. Das and M. Barma, Particles sliding on a fluctuating surface: Phase separation and power laws, Phys. Rev. Lett. **85**, 1602 (2000).

[60] S. Mishra and S. Ramaswamy, Active nematics are intrinsically phase separated, Phys. Rev. Lett. **97**, 090602 (2006).

[61] A. Das, A. Polley, and M. Rao, Phase segregation of passive advective particles in an active medium, Phys. Rev. Lett. **116**, 068306 (2016).

[62] A. I. Curatolo, N. Zhou, Y. Zhao, C. Liu, A. Daerr, J. Tailleur, and J. Huang, Cooperative pattern formation in multi-component bacterial systems through reciprocal motility regulation, Nat. Phys. **16**, 1152 (2020).

[63] S. Gude, E. Pince, K. M. Taute, A. B. Seinen, T. S. Shimizu, and S. J. Tans, Bacterial coexistence driven by motility and spatial competition, Nature (London) **578**, 588 (2020).

[64] L. Laganenka and V. Sourjik, Autoinducer 2-Dependent *Escherichia coli* biofilm formation is enhanced in a dual-species coculture, Appl. Environ. Microbiol. **84**, e02638-17 (2018).

[65] A. R. Muok and A. Briegel, Intermicrobial hitchhiking: How nonmotile microbes leverage communal motility, Trends Microbiol. **29**, 542 (2021).

[66] See Supplemental Material at http://link.aps.org/supplemental/10.1103/PRXLife.2.023002 for additional Figs. S1–S11, Tables S1–S3, Movies 1–5, and supplementary note.

[67] B. E. Scharf, K. A. Fahrner, L. Turner, and H. C. Berg, Control of direction of flagellar rotation in bacterial chemotaxis, Proc. Natl. Acad. Sci. USA **95**, 201 (1998).

[68] C. P. Royall, J. Dzubiella, M. Schmidt, and A. van Blaaderen, Nonequilibrium sedimentation of colloids on the particle scale, Phys. Rev. Lett. **98**, 188304 (2007).

[69] A. Wysocki, C. P. Royall, R. G. Winkler, G. Gompper, H. Tanaka, A. v. Blaaderen, and H. Löwen, Direct observation of hydrodynamic instabilities in a driven non-uniform colloidal dispersion, Soft Matter **5**, 1340 (2009).

[70] P. J. Mucha, S. Y. Tee, D. A. Weitz, B. I. Shraiman, and M. P. Brenner, A model for velocity fluctuations in sedimentation, J. Fluid Mech. **501**, 71 (2004).

[71] J. P. Hernandez-Ortiz, J. J. de Pablo, and M. D. Graham, N log n method for hydrodynamic interactions of confined polymer systems: Brownian dynamics, J. Chem. Phys. **125**, 164906 (2006).

[72] K. Drescher, K. C. Leptos, I. Tuval, T. Ishikawa, T. J. Pedley, and R. E. Goldstein, Dancing volvox: Hydrodynamic bound states of swimming algae, Phys. Rev. Lett. **102**, 168101 (2009).

[73] A. P. Petroff, X. L. Wu, and A. Libchaber, Fast-moving bacteria self-organize into active two-dimensional crystals of rotating cells, Phys. Rev. Lett. **114**, 158102 (2015).

[74] O. Schauer, B. Mostaghaci, R. Colin, D. Hurtgen, D. Kraus, M. Sitti, and V. Sourjik, Motility and chemotaxis of bacteria-driven microswimmers fabricated using antigen 43-mediated biotin display, Sci. Rep. **8**, 9801 (2018).

[75] M. Molaei, M. Barry, R. Stocker, and J. Sheng, Failed escape: Solid surfaces prevent tumbling of *Escherichia coli*, Phys. Rev. Lett. **113**, 068103 (2014).

[76] R. Matas-Navarro, R. Golestanian, T. B. Liverpool, and S. M. Fielding, Hydrodynamic suppression of phase separation in active suspensions, Phys. Rev. E **90**, 032304 (2014).

[77] D. Saintillan and M. J. Shelley, Instabilities and pattern formation in active particle suspensions: Kinetic theory and continuum simulations, Phys. Rev. Lett. **100**, 178103 (2008).

[78] F. Guzmán-Lastra, H. Löwen, and A. J. T. M. Mathijssen, Active carpets drive non-equilibrium diffusion and enhanced molecular fluxes, Nat. Commun. **12**, 1906 (2021).

[79] D. Grober, I. Palaia, M. C. Uçar, E. Hannezo, A. Saric, and J. Palacci, Unconventional colloidal aggregation in chiral bacterial baths, Nat. Phys. **19**, 1680 (2023).

[80] M. Huang, W. Hu, S. Yang, Q. X. Liu, and H. P. Zhang, Circular swimming motility and disordered hyperuniform state in an algae system, Proc. Natl. Acad. Sci. USA **118**, e2100493118 (2021).

[81] A. J. T. M. Mathijssen, F. Guzman-Lastra, A. Kaiser, and H. Lowen, Nutrient transport driven by microbial active carpets, Phys. Rev. Lett. **121**, 248101 (2018).

[82] H. R. Xu, J. Dauparas, D. Das, E. Lauga, and Y. L. Wu, Self-organization of swimmers drives long-range fluid transport in bacterial colonies, Nat. Commun. **10**, 1792 (2019).

[83] W. Gilpin, M. S. Bull, and M. Prakash, The multiscale physics of cilia and flagella, Nat. Rev. Phys. **2**, 74 (2020).

[84] N. Darnton, L. Turner, K. Breuer, and H. C. Berg, Moving fluid with bacterial carpets, Biophys. J. **86**, 1863 (2004).

[85] D. O. Serra, A. M. Richter, G. Klauck, F. Mika, and R. Hengge, Microanatomy at cellular resolution and spatial order of physiological differentiation in a bacterial biofilm, mBio **4**, e00103-13 (2013).

[86] S. I. Jensen, R. M. Lennen, M. J. Herrgård, and A. T. Nielsen, Seven gene deletions in seven days: Fast generation of *Escherichia coli* strains tolerant to acetate and osmotic stress, Sci. Rep. **5**, 17874 (2015).

[87] E. Amann, B. Ochs, and K.-J. Abel, Tightly regulated tac promoter vectors useful for the expression of unfused and fused proteins in *Escherichia coli*, Gene **69**, 301 (1988).

[88] O. Besharova, V. M. Suchanek, R. Hartmann, K. Drescher, and V. Sourjik, Diversification of gene expression during formation of static submerged biofilms by *Escherichia coli*, Front. Microbiol. **7**, 1568 (2016).

[89] J. Schwarz-Linek, J. Arlt, A. Jepson, A. Dawson, T. Vissers, D. Miroli, T. Pilizota, V. A. Martinez, and W. C. K. Poon, *Escherichia coli* as a model active colloid: A practical introduction, Coll. Surf. B **137**, 2 (2016).

[90] www.microparticles-shop.de

[91] https://fiji.sc/

[92] DOI:10.5281/zenodo.3516258

[93] S. Dey, D. Das, and R. Rajesh, Spatial structures and giant number fluctuations in models of active matter, Phys. Rev. Lett. **108**, 238001 (2012).

[94] D. Legland, I. Arganda-Carreras, and P. Andrey, MorphoLibJ: Integrated library and plugins for mathematical morphology with ImageJ, Bioinformatics **32**, 3532 (2016).

[95] I. F. Sbalzarini and P. Koumoutsakos, Feature point tracking and trajectory analysis for video imaging in cell biology, J. Struct. Biol. **151**, 182 (2005).

[96] L. G. Wilson, V. A. Martinez, J. Schwarz-Linek, J. Tailleur, P. N. Pusey, W. C. K. Poon, and G. Bryant, Differential dynamic microscopy of bacterial motility, Phys. Rev. Lett. **106**, 018101 (2011).

[97] DOI:10.5281/zenodo.7781880

[98] V. M. Suchanek, M. Esteban-López, R. Colin, O. Besharova, K. Fritz, and V. Sourjik, Chemotaxis and cyclic-di-GMP signalling control surface attachment of *Escherichia coli*, Mol. Microbiol. **113**, 728 (2020).

[99] https://github.com/croelmiyn/SimulationMixtures

[100] https://gitlab.gwdg.de/remy.colin/SimulationMixtures, DOI:10.5281/zenodo.10839746